

Origin of Topological Order in a Cooper Pair Insulator

Siddhartha Patra* and Siddhartha Lal†

Department of Physical Sciences, Indian Institute of Science Education and Research-Kolkata, W.B. 741246, India

(Dated: February 26, 2021)

While a topologically ordered counterpart of the s-wave superconductor has been proposed in the literature on phenomenological grounds, its microscopic origin remains unknown. In meeting this goal, we employ the recently developed unitary renormalisation group (URG) method on a generalised model of electrons in two spatial dimensions with attractive interactions. We show that the effective Hamiltonian obtained at the stable low-energy fixed point of the RG flow corresponds to a gapped, insulating state of quantum matter we call the Cooper pair insulator (CPI). Detailed analyses show that the CPI ground state manifold displays several signatures of topological order, including a four-fold degeneracy when placed on the torus. Spectral flow based arguments reveal the emergent gauge-theoretic structure of the effective theory: the CPI effective Hamiltonian can be written entirely in terms of non-local Wilson loops. Further, it contains a topological θ -term whose coefficient is quantised in keeping with the requirement of invariance of the ground state under large gauge transformations. This θ -term is known to be equivalent to the Chern-Simons term in two spatial dimensions. Passage from the CPI to the metal by tuning the θ coefficient reveals a plateau structure of the CPI ground state in terms of the steadily decreasing number of condensed Cooper pairs. Investigations reveal that the long-ranged many-particle entanglement content of the CPI ground state is driven by inter-helicity two-particle scattering processes. The plateau with $\theta = 0$ possesses the largest bipartite entanglement entropy (EE), scaling logarithmically with subsystem size (L) and falling rapidly upon tuning θ towards the metal. The bipartite EE for inter-plateau transitions shows universal signatures in its variations with L and θ . While the EE signatures for plateaux and transitions can be distinguished at low temperatures, such distinctions are smeared out as temperature is raised. We also study the passage from the CPI to the s-wave BCS superconducting ground state under RG, and find that the RG flow promotes fluctuations in the number of condensed Cooper pairs and lowers those in the conjugate global phase of the ground state wavefunction. Consequently, we find that the distinct signatures of long-ranged entanglement in the CPI are replaced by the well-known short-ranged entanglement of the BCS state. Analysing the effects of Josephson effects reveals that while a Cooper pair tunnel coupling between two CPI systems does not lead to phase stiffening, breaking the global $U(1)$ phase rotation symmetry in one of them induces a phase coherence in the other. However, the generation of a Josephson current requires the separate breaking of the $U(1)$ symmetry in the two systems. Finally, we study the renormalisation of the entanglement in k -space for both the CPI and BCS ground states. The topologically ordered CPI state is shown to possess an emergent hierarchy of scales of entanglement, and that this hierarchy collapses in the BCS state. Our work offers clear evidence for the microscopic origins of topological order in this prototypical system, and lays the foundation for similar investigations in other systems of correlated electrons.

CONTENTS

I. Introduction	1	B. The effect of a Josephson coupling	17
II. Effective theory of the Cooper Pair Insulator (CPI)	4	VI. Entanglement Renormalisation	17
III. Topological Features of CPI	6	VII. Conclusions and Discussions	20
A. Topological nature of the effective theory	6	Acknowledgments	21
B. Topological degeneracy at $\Phi = 0$.	8	A. Hamiltonian RG	22
C. Spectral flow, plateau ground states and topological quantum numbers	9	B. URG with symmetry breaking field	23
IV. Entanglement Features of CPI	10	References	23
A. Entanglement Spectrum	10		
B. Entanglement Entropy of the plateau ground states and transitions	12		
V. Passage to the BCS ground state	14		
A. Properties of the ground state	14		

I. INTRODUCTION

Superconductivity is undoubtedly one of the best studied example of an emergent collective phenomenon in a system of interacting electrons. While Cooper's theory¹

arXiv:2102.12193v2 [cond-mat.str-el] 25 Feb 2021

demonstrates that the presence of an attractive pairing interaction can lead to the formation and condensation of two-electron bound states (Cooper pair), the celebrated BCS theory² well describes the superconducting nature of this condensate of Cooper pairs in terms of a ground state wavefunction with a fluctuation in the number of Cooper pairs. Importantly, the BCS theory provides microscopic insight into various superconducting properties like the Meissner-Ochsenfeld effect, phase stiffness and the supercurrent, the transition temperature etc. The phenomenological Ginzburg Landau theory³ captures well the criticality of the superconducting transition in terms of a second order transition, involving the spontaneous breaking of the global $U(1)$ symmetry of the electronic Hamiltonian; this is known to be equivalent to the abelian Higgs field theory. The many-particle entanglement properties of the BCS wavefunction have also been established more recently^{4,5}.

In the presence of a magnetic field^{6–8} and/or disorder^{9–11}, a superconducting thin film has been observed to undergo a transition to an insulating state of matter (see Ref.¹² for a review). Several experimental^{13,14} and theoretical^{15,16} works offer evidence shows that this insulator^{17,18} has Cooper pairs present in it. Recent experiments^{19–33} reveal the existence of an intervening metallic phase, called the “Bose metal” phase³⁴, lying between the superconducting and insulating phases. Despite considerable effort, the precise nature of such a Bose metal remains unclear. Notable among various theoretical efforts on the Bose metal is the development of a gauge theory of Josephson junction arrays (JJA)^{35,36}, which show the Bose metal can be described by a topological Chern-Simons field theory emerging out of the nonlocal interaction between the quasiparticle and vortex excitations of the superconducting system. Diamantini et al.³⁷ show that such a topological insulating phase possesses, at finite temperatures, a longitudinal conductance mediated by time-reversal symmetry preserved counter-propagating edge modes. Hansson et al.³⁸ further established that the abelian Higgs model equivalent of the s-wave superconductor possesses other important features of topological order, i.e., a nontrivial ground state degeneracy revealed on a multiply connected spatial manifold (such as a torus) and charge fractionalization. The degenerate ground states are labelled by topological quantum numbers corresponding to the eigenvalues of Wilson and ’t-Hooft loops^{38–40}. More recently, the authors of Ref.⁴¹ have shown that the gapped topological bulk for s-wave pairing does not possess gapless edge states. Indeed, such a state displays a vanishing Hall conductance. Further, they also study the nature of the topological order in other spin-singlet superconductors⁴¹. The Cooper pair insulating phase has also been studied in lattice bosonic superconductors using vortex-boson duality^{42,43}, and its topological order investigated in the two dimensional variant⁴⁴.

Insight into such a topologically ordered insulating phase (or Bose metal) from a microscopic approach, however,

remains to be developed. Indeed, this is the primary goal of this work. Thus, we are going to present microscopic Hamiltonian for this novel phase of quantum matter, demonstrating it to be an insulator with topological ordered gapped ground state manifold. Importantly, we will find that such a state is emergent purely from quantum fluctuations arising from inter-particle interactions. Further, such quantum fluctuations preserve translational and time-reversal invariance, and are not necessarily driven by either disorder or the coupling to an external magnetic field.

In meeting this goal, we begin with a generalized Hamiltonian for a Fermi liquid with a short-ranged repulsive density-density interaction, as well as attractive pairing term. Suitably rewritten in terms of Anderson pseudospins⁴⁵, this corresponds to a reduced BCS Hamiltonian with additional repulsive interactions familiar from Fermi liquid theory. Then, using the unitary renormalization group (URG) technique recently developed by some of us^{46–51}, we resolve in a step-wise manner the quantum fluctuations arising from the non-commutativity between the kinetic energy of the electrons and the inter-particle interactions. This involves decoupling one electronic Fock state in the momentum space from all the other states it was connected to, such that the occupation number of the decoupled state is rendered as an integral of motion. The decoupling proceeds in a hierarchical fashion in terms of the kinetic energies of the electrons, from high (near the Brillouin zone edge, UV) to low (near the Fermi surface, IR), and an effective Hamiltonian is generated at every step. For the sake of clarity, we have encapsulated the major aspects of the URG method in Appendix A. As shown in Sec. II, the RG flow stops at an IR fixed point, yielding a low energy effective theory of a fixed number of condensed Cooper pairs but without any breaking of the macroscopic $U(1)$ phase (i.e., with vanishing phase stiffness).

We find that the emergent fixed point effective theory (eq.(11)) involves a non-local renormalised interaction between all pseudospins within the window that is emergent in k -space around the erstwhile Fermi surface, and described by a collective zero-mode degree of freedom comprised of these pseudospins. We call this symmetry unbroken phase of condensed Cooper pairs as the *Cooper Pair Insulator* (CPI). The RG procedure involves a novel energy scale for quantum fluctuations (ω). In keeping with this, the RG phase diagram obtained in Fig.1 clearly displays a quantum phase transition separating a CPI phase (at low ω) and a gapless Fermi liquid metal (at higher ω) for any repulsive interaction. The CPI Hamiltonian corresponds to a collective quantum rotor model coupled to an effective Aharonov-Bohm (AB) flux (Φ). We demonstrate that there exist different ground states of this CPI Hamiltonian related to one another by spectral flow upon tuning Φ , and displays the emergent quantisation of Φ under the RG flow. Importantly, we gain an idea of the accuracy of our method by numerically benchmarking the energy per particle of the ground state

(eq.(15)) of the CPI Hamiltonian obtained in the thermodynamic limit with that obtained from exact diagonalisation calculations (Fig.2).

We have studied the topological features of the CPI Hamiltonian in Sec.III. We establish first the gauge theoretic nature of the emergent effective IR theory obtained from the RG by demonstrating that the collective Hamiltonian for the CPI can be written completely in terms of a nonlocal Wilson loop operator. This is not surprising, given the zero-dimensional nature of the effective Hamiltonian, where all degrees of freedom (within the emergent IR window in momentum space) are interacting with one another. The CPI Hamiltonian contains an topological θ -term for a non-zero effective AB flux^{52,53}. As shown by Yao and Lee⁵⁴, this zero-dimensional θ -term is in correspondence to a $U(1)$ Chern-Simons topological term in two spatial dimensions. This establishes the effective theory for the CPI as the microscopic origin of the phenomenological $U(1)$ Chern-Simons gauge theories obtained by various people earlier^{35,36,38,41}. We then reveal the nontrivial topological degeneracy and charge fractionalization signatures of the topologically ordered CPI ground state manifold through a flux-insertion spectral flow argument^{48,50,55,56}. These spectral flow arguments reveal a plateaux-like quantisation of the number of Cooper pairs (N , a topological quantum number) upon tuning Φ through integer values (Fig.4), with the passage between the plateaux signifying topological transitions (at half-integer values of Φ). The collapse of the energy spectrum of the CPI phase with increasing Φ (Fig.5) yields another view of the transition between the CPI and metallic phases. As shown in Fig.6, the CPI state is found to possess large helicity cross-correlations (Υ , a signature of inter-helicity two-particle scattering processes). Finally, in Fig.7, we track the passage into the CPI ground state by starting from a finite (but small) temperatures and lowering towards $T = 0$.

In Sec.IV, we present a detailed analysis of the entanglement features of the CPI ground state. The entanglement spectrum (ES) computed for the lowest CPI ground state ($\Phi = 0$) is found to be doubly degenerate for all partitions of the system (Fig.8), reflecting the additional particle-hole symmetric nature of this CPI ground state. This degeneracy is lifted at the first topological transition ($\Phi = 1/2$, Fig.8). Interestingly, all other CPI ground states (corresponding to non-zero positive integer values of Φ) are observed to show the degeneracy of the ES for only the equipartitioned system (Fig.9); the degeneracy is again lifted at the transitions. We find that the bipartite entanglement entropy (EE) has a logarithmic dependence on the subsystem length L (Fig.10). Further, Fig.11 shows that the $\Phi = 0$ plateau possesses the largest EE, and that this is rapidly lowered to zero as Φ is tuned through various plateaux towards the gapless metal. The topological transitions between the CPI ground states display universal signatures in the variations of their EE with system size L and flux Φ : EE shows a non-monotonic variation with L (Fig.12), with

a peak value at $L \equiv L^*$ that is universal as Φ is tuned (Fig.13). Further, for $L < L^*$, the EE versus L data falls onto a universal curve (Fig.12). Finally, L^* approaches the equipartition value at Φ is tuned close to the transition between the CPI state and the metal (Fig.13). Variations of the EE for the CPI ground states and the transitions with temperature also show interesting signatures (Fig.14). The EE versus temperature curves for all values of Φ corresponding to a given ground state finally merge at $T \rightarrow 0$. Further, the EE curves for all transitions are clearly distinct from those associated with the CPI ground states. Interestingly, for large temperatures, the dominance of thermal fluctuations in smearing out the distinction between the CPI ground states and the transitions can be seen in the fact that *all* EE curves have a linear variation against temperature and with a universal slope.

Having studied the topologically ordered CPI phase in detail, in in Sec.V, we turn to its connection with the symmetry broken BCS ground state. We note that the low energy effective theory for the CPI phase corresponds to an isotropic Lipkin-Meshkov-Glick (LMG) model⁵⁷⁻⁵⁹. Recent studies^{60,61} have also revealed the existence of such an effective Hamiltonian within the global $U(1)$ symmetry broken BCS phase, arising from degrees of freedom that are singular under the Bogoliubov-Valatin transformation and corresponding to a “thin spectrum” or Anderson tower of states⁶². Upon taking the system size to the thermodynamic limit, the collapse of this thin spectrum is believed to engender the spontaneous breaking of the $U(1)$ symmetry. On the other hand, it is believed that in a mesoscopic superconducting grain, the presence of a large charging term helps in making the thin spectrum robust⁶³. Thus, in Appendix B, we investigate the passage from the CPI phase to the BCS phase under RG upon adding a global $U(1)$ symmetry breaking term in the CPI Hamiltonian.

In keeping with this, we show in Fig.15 of Sec.V that the $U(1)$ symmetry breaking field promotes fluctuations in the number of Cooper pairs, while lowering the fluctuations in the conjugate global phase. Further, in Fig.16, we show that symmetry breaking effectively destroys the helicity cross-correlation (Υ) among the Cooper-pairs under RG. The BCS wavefunction is a product state in momentum space, with vanishing inter- k entanglement between Cooper pairs and maximum inter-spin entanglement due to the singlet configuration of each pair^{4,5}. We find that an increasing symmetry breaking field lowers the inter- k entanglement between Cooper pairs present in the CPI to zero, while raising the inter-spin entanglement to its BCS value (Fig.17). Further, the equal-size partitioned entanglement entropy shows a monotonic decrease of entanglement for the CPI ground states (and their intervening transitions) with an increasing symmetry breaking field (Fig.18), while the metallic phase shows a non-monotonic variation.

Another way by which to distinguish the CPI phase from the BCS superconductor lies in investigating the effects of

a Josephson coupling. Thus, in a second part of Sec.V, we consider the case of two CPI systems whose bulk is coupled via Josephson coupling (i.e., we are ignoring all effects from gapless edge states), and one of whom is placed in an $U(1)$ symmetry breaking field. In Fig.19, we find that while a Josephson coupling between two pure CPI systems (i.e., with the symmetry breaking of the second CPI system switched off) does not lead to any phase stiffness in another another, breaking the symmetry in one of them does give a proximity induced phase coherence in the other. Indeed, an increasing symmetry breaking field together with a large Josephson coupling turn a CPI into a phase stiff ground state. The generation of a Josephson current through the phase-locking, however, requires the separate symmetry breaking of the two individual subsystems. This is demonstrated in Fig.20, through the observation of a periodic variation of the ground state energy $E(\phi)$ with the phase difference ϕ upon the introduction of separate non-zero symmetry breaking fields in both CPI systems. In addition to the recent transport measurements of Ref.37 on the Bose metal, these findings serve as predictions for the experimental search of the CPI state of quantum matter.

Next, in Sec.VI, we have carried out an entanglement RG using the technique developed by us in Refs.51,64. This strategy can be described briefly as follows. Our URG analysis has helped obtain the IR fixed point Hamiltonians for the CPI and BCS phases, their ground state wavefunctions as well as the unitary transformations of the RG flow that led to them. for corresponding CPI and BCS wavefunctions. The quantum circuits corresponding to these unitary transformations is shown for the CPI and BCS cases in Figs.21 and 22 respectively. Now, applying these unitary operations in reverse on a given IR wave function, we obtain a family of wave functions under RG leading towards that pertaining to the UV theory. We compute the entanglement entropy of various sizes of partitions from this set of wavefunctions, revealing the evolution of the entanglement entropy with RG. As shown in Fig.23, the EE for the constituent sub-blocks of the emergent CPI ground state are clearly distinguished from that for all other partitions: their EE varies little under RG from UV to IR, while that of all others is lowered under RG from UV to IR. Further, this analysis reveals a remarkable hierarchy of scales of entanglement possessed by the CPI ground state. This hierarchy of scales of entanglement gradually collapses upon tuning a symmetry breaking field (Fig.24), until it is no longer present in the BCS ground state (Fig.25). Further, we can distinguish scaling towards the BCS and CPI ground states under RG flow. Finally, we conclude in Sec.VII with a discussion of some future directions.

II. EFFECTIVE THEORY OF THE COOPER PAIR INSULATOR (CPI)

We begin by deriving an effective Hamiltonian for an insulating state of matter comprised of a fixed number of Cooper pairs (referred to as the Cooper pair insulator, or CPI, in the introduction). For this, we will carry out a renormalisation group (RG) calculation on a system of electrons in two dimensions with a generalised pairing Hamiltonian, $H = \sum_q H_{\text{pair}}^q$, where

$$H_{\text{pair}}^q = \sum_k \epsilon_k n_k - \sum_{k \neq k', \sigma} |W_{kk'}^q| c_{k-q, \sigma}^\dagger c_{-k, -\sigma}^\dagger c_{-k', -\sigma} c_{k'-q, \sigma} + U \sum_{k \neq k'} (n_k - 1/2)(n_{k'} - 1/2), \quad (1)$$

where with q denotes the pair-momenta, ϵ_k the kinetic energy for electrons about a circular Fermi surface, $-|W_{kk'}^q|$ is the attractive pairing interaction, $U (> 0)$ a repulsive density-density interaction and $n_k = \sum_\sigma c_{k, \sigma}^\dagger c_{k, \sigma}$. Note that the case of a constant $|W_{kk'}^q| \forall (k, k', q)$ corresponds to the attractive Hubbard model⁶⁵. We proceed by using Anderson's pseudospin construction in the subspace $n_{k-q, \uparrow} = n_{-k, \downarrow}$:

$$\vec{S}_k = \frac{1}{2} \phi_k \cdot \vec{\tau} \cdot \phi_k^\dagger, \quad (2)$$

where $\vec{\tau} = (\tau^z, \tau^x, \tau^y)$ are the Pauli matrices and $\phi_k = (c_{k\uparrow}, c_{-k\downarrow}^\dagger)$. The pseudospins obey the standard commutation relation for spin-1/2: $[S_k^i, S_k^j] = i\epsilon_{jkl} S_k^l$. Then, we write H_{pair}^q as

$$H_{\text{pair}}^q = - \sum_k \tilde{\epsilon}_{k,q} (S_{k,q}^z - \frac{1}{2}) - \sum_{k \neq k'} \frac{|W_{kk'}^q|}{2} (S_{k,q}^- S_{k',q}^+ + \text{h.c.}) + U \sum_{k \neq k'} S_{k,q}^z S_{k',q}^z, \quad (3)$$

where $\tilde{\epsilon}_{k,q} = \epsilon_{-k} + \epsilon_{k+q}$ is the kinetic energy for a pair of electrons. In order to ensure the extensivity of the model, $|W_{kk'}^q| = |W_{kk'}^q|/N$ (where N corresponds to the total number of pseudospins, and hence $2N$ the total number of electrons). The special case of $H_{\text{pair}}^{q=0}$ with $|W_{kk'}^{q=0}|$ and $U = 0$ is called the Richardson pairing model (see Ref.66 and references therein).

Following the strategy developed in Refs.46-51, we now carry out a renormalisation group analysis on H_{pair}^q ; see appendix A for details. The RG equations obtained for $\tilde{\epsilon}$ and $|W_{kk'}^q|$ are

$$\frac{\Delta \tilde{\epsilon}_{k',q}^{(j)}}{\Delta \log \frac{\Lambda_j}{\Lambda_0}} = \frac{1}{4} \frac{|W_{k\Lambda k'}^{(j)}|^2}{\left(\omega - \frac{\epsilon_{k\Lambda, q}^{(j)}}{2} - \frac{U}{4} \right)}, \quad (4)$$

$$\frac{\Delta |W_{k'k''}^{q,(j)}|}{\Delta \log \frac{\Lambda_j}{\Lambda_0}} = -\frac{1}{4} \frac{|W_{k\Lambda k'}^{q,(j)}| |W_{k\Lambda k''}^{q,(j)}|}{\left(\omega - \frac{\epsilon_{k\Lambda, q}^{(j)}}{2} - \frac{U}{4} \right)}, \quad (5)$$

where the index (j) represents the RG step number, $|W_{k'k''}^{q,(j)}| = |V_{k'k''}^{q,(j)}|/N^{(j)}$ (for $N^{(j)}$ being the number of remnant pseudospins at the j^{th} RG step) and k_Λ the momentum at a k -space window (Λ) lying on a radial and around the circular Fermi surface. The symbol ω represents an energy scale for the quantum fluctuations that lead to UV-IR mixing. Further, we note that the RG step index j starts from the number of pseudospin (N) lying within the bare window Λ_0 and proceeds to smaller values. At every step of the RG, a pseudospin with momentum k_Λ lying on a given direction radial to the Fermi surface is disentangled from the rest ($\forall k < k_\Lambda$); the $U(1)$ symmetry of the circular Fermi surface ensures that the RG is carried out simultaneously for all pseudospins with momentum k_Λ . Note that the repulsive coupling U does not flow under RG, as two-particle quantum fluctuations do not lead to the renormalisation of this term. Instead, it appears as a Hartree-shift in the pseudospin Greens function $G_{ps} = [\omega - \frac{\tilde{\epsilon}_{k_\Lambda,q}^{(j)}}{2} - \frac{U}{4}]^{-1}$ present in the RG equations given above⁴⁶⁻⁵¹.

It can be seen that the normalization for $\tilde{\epsilon}_{k',q}^{(j)}$ is RG relevant for $\omega > (\tilde{\epsilon}_{k_\Lambda,q}/2 + U/4)$, while that for $|W_{k'k''}^{q,(j)}|$ is RG relevant for $\omega < (\tilde{\epsilon}_{k_\Lambda,q}^{(j)}/2 + U/4)$. Given that $\epsilon_{-k} = \epsilon_k$ for a circular Fermi surface, it is easily seen that $\tilde{\epsilon}_{k,q}^{(j)} \geq 2\epsilon_k^{(j)}$. Therefore, given the denominator $\omega - \tilde{\epsilon}_{k_\Lambda,q}^{(j)}/2 - U/4$ in both RG equations, the leading RG relevant q -sector for the lowest quantum fluctuation energyscale ($\omega = 0$) corresponds to the case of $q = 0$ (i.e., Cooper pairs with zero centre of mass momentum). Thus, we will henceforth study only the case of $\tilde{\epsilon}_{k,q=0}^{(j)} \equiv \tilde{\epsilon}_k^{(j)} = 2\epsilon_k^{(j)}$ and $H_{\text{pair}}^{q=0} \equiv H_{\text{pair}}^0$.

We define mode decompositions of the dispersion $\epsilon_k^{(j)}$ and the pairing coupling $|V_{kk'}^{(j)}|$ as follows

$$\tilde{\epsilon}_l^{(j)} = \frac{1}{\sqrt{N^{(j)}}} \sum_{\vec{k}} e^{i\vec{k}l} \epsilon_k^{(j)}, \quad \bar{V}_{l'l'}^{(j)} = \frac{1}{N^{(j)}} \sum_{k,k'} e^{i(kl+k'l')} |V_{kk'}^{(j)}| \quad (6)$$

such that the RG equations for $\tilde{\epsilon}_{l=0}^{(j)}$ and $\bar{V}_{l=0,l'=0}^{(j)}$ are observed to dominate under the RG flow over all other modes for a thermodynamically large system :

$$\text{Re} \left(\frac{\Delta \tilde{\epsilon}_{l=0}^{(j)}}{\Delta \tilde{\epsilon}_{l \neq 0}^{(j)}} \right) > 1, \quad \text{Re} \left(\frac{\Delta \bar{V}_{l=0,l'=0}^{(j)}}{\Delta \bar{V}_{l \neq 0,l' \neq 0}^{(j)}} \right) > 1. \quad (7)$$

The zero mode $\tilde{\epsilon}_0^{(j)}$ is related to the center of mass kinetic energy $\bar{\epsilon}^{(j)}$: $\tilde{\epsilon}_0^{(j)} = (\sum_k \epsilon_k^{(j)})/\sqrt{N^{(j)}} = \sqrt{N^{(j)}} \bar{\epsilon}^{(j)}$. Similarly, the zero mode $\bar{V}_{00}^{(j)}$ is connected to it's center of mass value : $\bar{V}^{(j)} = (\sum_{kk'} V_{kk'}^{(j)})/(N^{(j)})^2 = V_{00}^{(j)}/N^{(j)}$. Thus, the RG relations of these zero modes is equivalent to the study of the center of mass degrees of freedoms

$$\Delta \bar{\epsilon}^{(j)} = \frac{1}{4} \frac{|\bar{W}^{(j)}|^2}{\left(\omega - \frac{\bar{\epsilon}^{(j)}}{2} - \frac{U}{4} \right)} = -\Delta |\bar{W}^{(j)}|, \quad (8)$$

where $\bar{W}^{(j)} = \bar{V}^{(j)}/N^{(j)}$. In this way, we observe below the emergence of the well known reduced BCS model² at the stable fixed point of the RG eq.(8).

The relation between the two RG equations (eq.(8)) leads to a RG invariant: $\bar{\epsilon}^{(j)} + |\bar{W}^{(j)}| = C$, $C \in \mathcal{R}$. From this invariant, it can now be seen that when the kinetic energy $\bar{\epsilon}$ is RG relevant, the attractive coupling $|\bar{W}|$ is RG irrelevant and vice versa. We can now write the effective Hamiltonian obtained at the stable fixed point of the RG flow as

$$H_{\text{coll}} = -\frac{2\bar{\epsilon}^*}{N^*} \sum_k (S_k^z - \frac{1}{2}) - \frac{\bar{V}^*}{2N^*} \sum_{k \neq k'} (S_k^+ S_{k'}^- + \text{h.c.}) + U \sum_{k \neq k'} S_{k,q}^z S_{k',q}^z, \quad (9)$$

where $\bar{\epsilon}^*$, \bar{V}^* and N^* are the fixed point values of $\bar{\epsilon}^{(j)}$, $\bar{V}^{(j)}$ and $N^{(j)}$ respectively reached at the endpoint of the RG flow (and $\bar{V}^*/N^* = C - \bar{\epsilon}^*$). Finally, by defining the composite pseudospin $\vec{S} = \sum_k \vec{S}_k$, we can rewrite the Hamiltonian H_{coll} (upto additive constants) as

$$H_{\text{coll}} = -\frac{2\bar{\epsilon}^*}{N^*} S^z - \frac{\bar{V}^*}{2N^*} (S^+ S^- + S^- S^+) + U S^z{}^2 = -\frac{2\bar{\epsilon}^*}{N^*} S^z - \frac{\bar{V}^*}{N^*} (S^2 - S^z{}^2) + U S^z{}^2. \quad (10)$$

While the first term arises from the electronic kinetic energy, the second the potential energy saved by the formation of pairs (i.e., the condensation energy) and the third represents the repulsive charging energy cost of the electrons that form the Cooper pairs. Note that the Hamiltonian eq.(9) has the global $U(1)$ symmetry of the generalised pairing Hamiltonian eq.(1). This is expected, as RG transformations are symmetry preserving.

We present the RG phase diagram below in Fig.1 by a numerical solution of the RG equations for the electronic dispersion along a radial to the circular Fermi surface being $\epsilon_k = 2t \cos(k)$, a bare window near the Fermi energy $v_F \Lambda_0 = 0.3t$, a constant bare attractive coupling $|V_{kk'}^q| = 4t/N$ and the total number of pseudospins $N = 51$. The phase diagram is presented in the plane of the effective quantum fluctuation energy scale ω and the repulsive coupling U (and both are in units of the kinetic energy bandwidth $4t$). It clearly shows that the Cooper pair insulator (CPI) is stabilised at lower values of ω for all U , and that a metallic phase (lying at higher values of ω) is obtained through a quantum phase transition into a gapless Fermi liquid metallic phase.

For the sake of simplicity, we will henceforth focus on the case of $U = 0$ ^{57-60,67}

$$H_{\text{coll}} = -\frac{2\bar{\epsilon}^*}{N^*} S^z - \frac{\bar{V}^*}{N^*} (S^2 - S^z{}^2), = \frac{\bar{V}^*}{N^*} (S^z - \Phi)^2 - \frac{\bar{V}^*}{N^*} S^2, \quad (11)$$

where $\Phi \equiv \bar{\epsilon}^*/\bar{V}^*$ and we have ignored a constant ($\propto (\bar{\epsilon}^*/N^*)^2$). Further, for N^* pseudospins, $0 \leq S(\in$

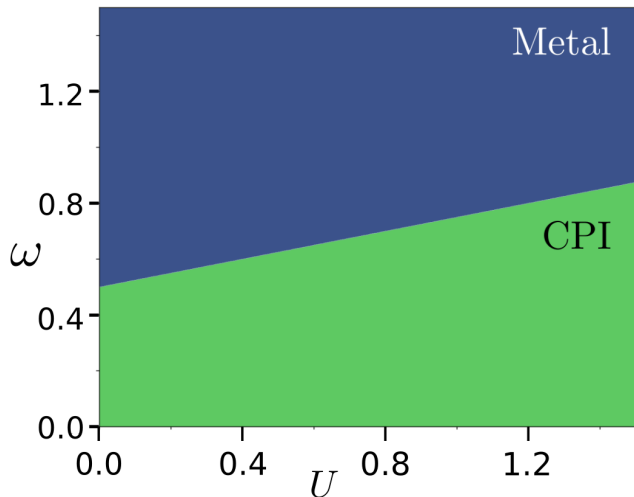


FIG. 1. Renormalisation group phase diagram for the effective pairing Hamiltonian given in eq.(3). The y-axis represents the energy scale (ω) for quantum fluctuations that are resolved under the RG flow, while the x-axis represents the repulsive interaction (U) in the parent metal (whose electrons feel the additional attractive pairing). The phase diagram clearly shows the existence of an emergent Cooper pair insulator (CPI) phase at low ω (i.e., energies proximate to the Fermi surface of the parent metal) for all $U \geq 0$.

\mathcal{Z}) $\leq N^*/2$, $-S \leq S^z (\in \mathcal{Z}) \leq S$ and the number of Cooper pairs is given by $N_c = S - S^z$. It is easily seen that both S and S^z commute with H_{coll} . Further, H_{coll} arises a global collective angular momentum degree of freedom, S^z , and possesses the form of a quantum particle whose dynamics is confined to a circle and coupled to an (effective) dimensionless Aharonov-Bohm (AB) flux Φ . As we will discuss in a later section, this points to a topological property possessed by the ground state manifold of its Hilbert space.

We note here, however, that the emergent Hilbert space corresponding to H_{coll} possesses the property of *spectral flow*. First, observe that minimisation of the energy is achieved under RG flow for the case of $\Phi = \bar{\epsilon}^*/\bar{V}^* \rightarrow 0+$ by a ground state possessing $S = N^*/2$ and $S^z = 0$, corresponding to the largest number of Cooper pairs ($N_c = N^*/2$). Spectral flow refers to the existence of ground states, corresponding to other positive integer values of S^z , that can be reached under RG for values of the effective AB flux $\Phi \gg 1$ flowing to the same positive integer. As we will now see, this emergent quantisation of the effective AB flux Φ under RG also provides a relation between the RG invariant C and the quantum fluctuation scale ω . As shown in Appendix A, the final fixed point value of $\bar{\epsilon}^*$ is given by $\bar{\epsilon}^* = 2\omega - \frac{U}{2}$. Using this together with the relation for the RG invariant is $C = \bar{\epsilon}^* + |\bar{W}|^*$, we find the effective flux at the IR fixed

point is

$$\Phi = \frac{\bar{\epsilon}^*}{|\bar{V}^*|} = \frac{2\omega - \frac{U}{2}}{N^*|\bar{W}^*|} = \frac{2\omega - \frac{U}{2}}{N^*(C - 2\omega + \frac{U}{2})} \equiv n \in \mathcal{Z} \quad (12)$$

For the case of $U = 0$, this leads to

$$C = 2\omega \left(\frac{1 + nN^*}{nN^*} \right) \rightarrow 2\omega \quad \text{for } n \gg 1. \quad (13)$$

Finally, we note that the ground state wavefunction of the $U(1)$ -symmetric CPI state with $S^z = 0$ (i.e., at strong coupling) is given by

$$|\psi_g\rangle = \mathcal{N} \left(\sum_k c_{-k\downarrow}^\dagger c_{k\uparrow}^\dagger \right)^S |\text{vac}\rangle \quad (14)$$

where $|\text{vac}\rangle$ is the state that contains no Cooper pairs, and \mathcal{N} is a normalisation factor. By acting with H_{coll} on $|\psi_g\rangle$, we obtain the ground state energy density as

$$\begin{aligned} \frac{E_g}{N^*} &= -\frac{\bar{V}^*}{N^{*2}} S^2 = -\frac{\bar{V}^*}{N^{*2}} \frac{N^*}{2} \left(\frac{N^*}{2} + 1 \right) \\ &= -\frac{\bar{V}^*}{4} \left(1 + \frac{2}{N^*} \right) \simeq -\frac{\bar{V}^*}{4} \quad \text{for } N^* \gg 1. \end{aligned} \quad (15)$$

In order to gauge the accuracy of the effective Hamiltonian (eq.(11)) and ground state wavefunction (eq.(14)) obtained from the RG procedure, we compare the ground energy density value obtained in the thermodynamic limit (eq.(15)) from a finite-size scaling analysis with that obtained from a finite-size scaling for exact diagonalization (ED) studies of small systems of the bare Hamiltonian (eq.(1)) for $U = 0$, $|V_{kk'}^q| = 2$ (in units of a hopping parameter t), $|W_{kk'}^q| = 2/N$. For a $U(1)$ -symmetric Fermi surface, it suffices to compare the energy density value obtained along any one diameter of the spherical Fermi volume. As is shown in Fig.2, we find excellent agreement between the results obtained in the thermodynamic limit from the two approaches: $E_g/N^* \simeq -0.254t$ from the RG, as against $E_g/N^* \simeq -0.252t$ obtained from ED. This indicates the efficiency of the RG method in preserving the spectral content during the flow towards the stable IR fixed point, and offers confidence in the analyses of subsequent sections that offer insight into the properties of the CPI phase.

III. TOPOLOGICAL FEATURES OF CPI

We will, in this section, study the topological properties of the many-body system described by the stable fixed point effective Hamiltonian H_{coll} (eq.(11)) obtained from the RG.

A. Topological nature of the effective theory

We begin by showing that the effective Hamiltonian for the plateau state in the strong coupling limit (i.e., with

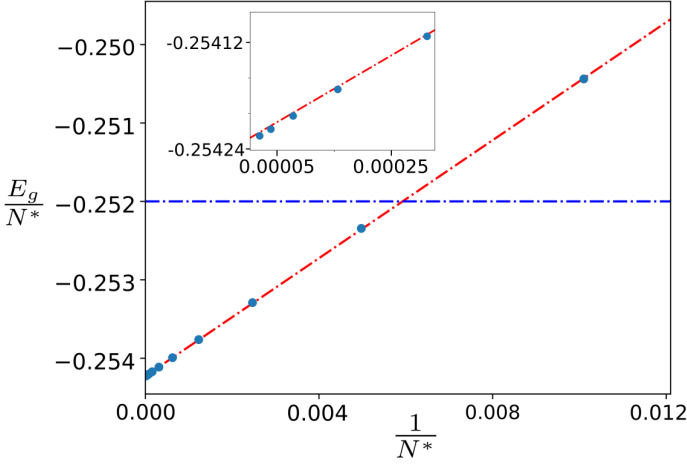


FIG. 2. Finite-size scaling of the ground state energy density E_g/N^* under RG for system sizes $N = 100, 202, 406, 814, 1600, 3200, 6400, 12800, 25600, 51200$ (blue circles from right to left). N^* is the number of pseudospins within the emergent subspace at the stable fixed point of the RG. The red dash-dot line shows a linear fit to the finite-size scaling data. The blue dash-dot line shows the thermodynamic limit value for E_g/N obtained from a finite-size scaling exact diagonalisation study of small systems ranging between 5 – 15 pseudospins. Inset: Zoom of RG finite-size scaling data for $N = 3200, 6400, 12800, 25600, 51200$.

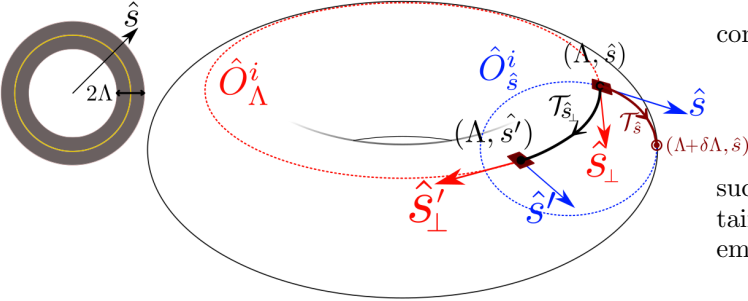


FIG. 3. (Left) Effective k -space window (dark grey) of size 2Λ around the Fermi surface (FS, yellow circle) formed under RG for the CPI phase. \hat{s} represents a given direction in k -space normal to the FS. (Right) Construction of the respective twist ($\hat{O}_{\hat{s}}, \hat{O}_{\Lambda}$) and translation operators ($\hat{T}_{\hat{s}}, \hat{T}_{\hat{s}_{\perp}}$) defined on the torus created by imposing periodic boundary conditions on emergent window in k -space (i.e., on all directions \hat{s}).

$\bar{\epsilon}^* = 0$) system) is purely topological. This will be done by rewriting $H_{coll}(\bar{\epsilon}^* = 0) = -\frac{\bar{V}^*}{N^*}(S_x^2 + S_y^2)$ in terms of emergent Wilson loop operators defined on a torus created by imposing periodic boundary conditions in the Λ -direction (i.e., the window in k -space that defines the CPI condensate, see Fig.3 below).

We define the k -space translation ($\mathcal{T}_{\hat{s}}$, brown curved line in Fig.3) and twist operators ($\hat{O}_{\hat{s}}^i$, blue dashed line in Fig.3)

$$\mathcal{T}_{\hat{s}} : S_{\Lambda, \hat{s}}^i \rightarrow S_{\Lambda + \delta\Lambda, \hat{s}}^i, \quad \hat{O}_{\hat{s}}^i = \exp\left[\frac{2\pi i}{N^*} i \sum_{n=0}^{N^*-1} n S_{n\Lambda, \hat{s}}^i\right] \quad (16)$$

where the twist operator $\hat{O}_{\hat{s}}^i$ spans all values of Λ in the \hat{s} direction, and imparts a gradual twist to the pseudospins $S_{n\Lambda, \hat{s}}^i$ such that the total twist imparted across the \hat{s} direction is 2π . Further, we can also define a composite twist operator that spans the entire torus shown in Fig.3

$$\tilde{O}^i = \prod_{n=0}^{N^*-1} \hat{O}_{R^n \hat{s}} = \exp\left[\frac{2\pi i}{N^*} \sum_{n,m=0}^{N^*-1} m S_{m\delta\Lambda, R^n \hat{s}}^i\right]. \quad (17)$$

Then, we compute the following (nonlocal) Wilson loop operator \mathcal{W}_1^i ($i = (x, y)$) defined in terms of $\mathcal{T}_{\hat{s}}$ and \tilde{O}^i

$$\begin{aligned} \mathcal{W}_1^i &= \mathcal{T}_{\hat{s}} \tilde{O}^i \mathcal{T}_{\hat{s}}^\dagger \tilde{O}^{i\dagger} = \exp\left[\frac{2\pi i}{N^*} \sum_{m,n=0}^{N^*-1} S_{m\Lambda, R^n \hat{s}}^i\right] \\ &\quad \times \exp\left[2\pi i \sum_{n=0}^{N^*-1} S_{\Lambda=0, R^n \hat{s}}^i\right], \quad (18) \end{aligned}$$

where the first term on the right hand side imparts the twist to the centre of mass of the torus of pseudospins. The second denotes the trivial phase twist accumulated at a virtual boundary defined on the torus by the curve $\Lambda = 0$, $\exp\left[2\pi i \sum_{n=0}^{N^*-1} S_{\Lambda=0, R^n \hat{s}}^i\right] = 1$. Thus, we obtain the composite pseudospin ($S^i, i = (x, y)$) in terms of \mathcal{W}_1^i as

$$S^i = \sum_{m,n} S_{m\Lambda, R^n \hat{s}}^i = \frac{N^*}{2\pi} \text{Im} [\ln(\mathcal{W}_1^i)], \quad (19)$$

such that the $U(1)$ -symmetric effective Hamiltonian obtained from the RG can be written purely in terms of the emergent \mathcal{W}_1^i as

$$H_{coll} = -\frac{\bar{\epsilon}^*}{\pi} \text{Im} [\ln(\mathcal{W}_1^z)] - \frac{N^* \bar{V}^*}{4\pi^2} \sum_{i=x,y} \left(\text{Im} [\ln(\mathcal{W}_1^i)] \right)^2 \quad (20)$$

This shows us that the $U(1)$ symmetry is encoded in the invariance of the Wilson loops \mathcal{W}_1^i large gauge transformations^{40,68}, and that the nonlocal nature of their dynamics is encoded in the dependence of H_{coll} on \mathcal{W}_1^i . In this way, we can clearly see the emergence of an effective gauge theory from the microscopic Hamiltonian eq.(1).

We note that H_{coll} can also be written in terms of another set of emergent Wilson loop operators \mathcal{W}_2^i obtained from a different pair of translation and twist operators defined on the torus (see Fig.3)

$$\mathcal{T}_{\hat{s}_{\perp}} : S_{\Lambda, \hat{s}}^i \rightarrow S_{\Lambda, R\hat{s}}^i, \quad \hat{O}_{\Lambda}^i = \exp\left[\frac{2\pi i}{N^*} i \sum_{n=0}^{N^*-1} n S_{\Lambda, R^n \hat{s}}^i\right], \quad (21)$$

such that we can redefine as earlier the following composite twist (\tilde{O}^i) and pseudospin (S^i) and the Wilson loop

\mathcal{W}_2^i as

$$\tilde{O}^i = \prod_{m=0}^{N^*-1} \hat{O}_{m\delta\Lambda} = \exp \left[\frac{2\pi}{N^*} i \sum_{n,m=0}^{N^*-1} m S_{m\delta\Lambda, R^n \hat{s}}^i \right], \quad (22)$$

$$S^i = \frac{N^*}{2\pi} \text{Im} [\ln(e^{i\pi} \mathcal{W}_2^i)] \quad , \quad \mathcal{W}_2^i = \mathcal{T}_{\hat{s}_\perp} \tilde{O}^i \mathcal{T}_{\hat{s}_\perp}^\dagger \tilde{O}^{i\dagger}. \quad (23)$$

We can once again write the effective Hamiltonian H_{coll} as

$$H_{coll} = -\frac{\bar{\epsilon}_2^*}{\pi} \text{Im} [\ln(\mathcal{W}_2^z)] - \frac{N^* \bar{V}^*}{4\pi^2} \sum_{i=x,y} \left(\text{Im} [\ln(\mathcal{W}_2^i)] \right)^2 \quad (24)$$

where $\bar{\epsilon}_2^* = \bar{\epsilon}^* - N^* V^*/2$.

The fact that the effective Hamiltonian (H_{coll}) obtained from the RG can be written completely in terms of global collective gauge degrees of freedom (i.e., the Wilson loops \mathcal{W}_1^i and \mathcal{W}_2^i) is not surprising. Indeed, following Refs.^{35,38} on the effective theory for the CPI phase being a Chern-Simons gauge field theory, we expect that the effective Hamiltonian for the CPI cannot be written in terms of local degrees of freedom. Thus, for finite and non-zero $\bar{\epsilon}^*$, the association of a $U(1)$ -symmetric Chern-Simons gauge field theory with the effective quantum rotor Hamiltonian H_{coll} (eq.(11)) in 0-spatial dimensions can be argued for as follows. The action corresponding to H_{coll} contains a 0-dimensional topological θ -term⁵²

$$\theta = i \frac{\bar{\epsilon}^* N^*}{V^*} \int_0^\beta d\tau \frac{\partial \phi}{\partial \tau}, \quad (25)$$

written in terms of a global phase ϕ conjugate to S^z , such that

$$-i\hbar \partial / \partial \phi \equiv S^z = -\frac{i}{\hbar} [S^x, S^y] = \frac{iN^{*2}}{4\pi\hbar} [\ln W_1^x, \ln W_1^y], \quad (26)$$

and with a Berry phase given by $\gamma = 2\pi \frac{\bar{\epsilon}^*}{V^*} = 2\pi\Phi$ ⁵². It was shown by Yao and Lee⁵⁴ that such a θ -term in 0-spatial dimensions is in precise correspondence with a $U(1)$ Chern-Simons topological term in 2-spatial dimensions. Hansson et al.³⁸ show that the Chern-Simons term encodes a topological coupling of the vorticity (or winding number part) of the global phase field ϕ to a field associated with the quasiparticle excitations. In this way, they show that the system, in the presence of a dynamical gauge field, possesses gauge invariance under large gauge transformations. Further, they argue that the time-reversal invariance of the original problem necessitates that the K -matrix of the equivalent 2-flavour mixed Chern-Simons theory is $K = 2\sigma_x$ (see also Ref.⁴¹). Then, the topological ground state degeneracy on a torus of genus g is given by $|Det(K)|^g = 4^g$ ⁴⁰. This clarifies that the topologically ordered condensate of vortices observed in Ref.³⁸, arising from the coupling the global phase of the superconducting ground state to dynamical electromagnetic gauge fields, corresponds to the Cooper pair number fixed insulating state of matter (the CPI phase) found at the stable fixed point of the RG flow. Next, we will demonstrate the 4-fold degeneracy for the special case of $\bar{\epsilon}^* = 0 = \Phi$.

B. Topological degeneracy at $\Phi = 0$.

In order to unveil a ground state degeneracy at $\Phi = 0$, we follow the adiabatic flux insertion treatment of Osikawa⁶⁹. For this, we define the following momentum translation ($\hat{\mathcal{T}}_{\hat{s}_\perp}$) (see Fig.3) and twist ($O_{ph}^{\hat{s}_\perp}$) operators

$$\hat{\mathcal{T}}_{\hat{s}_\perp} = e^{i\hat{\Theta}_{\hat{s}_\perp}}, \quad O_{ph}^{\hat{s}_\perp} = \exp \left\{ i \frac{2\pi}{N} \sum_{p=0}^{N-1} k S_{(Rp k_{\hat{s}})}^z \right\} \quad (27)$$

$$S_{(Rp k_{\hat{s}})}^z = \sum_{\Lambda(Rp k_{\hat{s}})} S_{\Lambda(Rp k_{\hat{s}})}^z, \quad (28)$$

where $\hat{\Theta}_{\hat{s}_\perp}$ denotes the center of mass angular position along \hat{s}_\perp . With this, we find

$$\mathcal{T}_{\hat{s}_\perp} O_{ph}^{\hat{s}_\perp} \mathcal{T}_{\hat{s}_\perp}^\dagger = O_{ph}^{\hat{s}_\perp} \exp \left[\frac{i2\pi}{N} \left(N S_0^z - \sum_{k_{\hat{s}}=0}^{N-1} S_{k_{\hat{s}}}^z \right) \right],$$

$$= O_{ph}^{\hat{s}_\perp} \exp \left[i\pi(2n+1) \right] = O_{ph}^{\hat{s}_\perp} e^{i\pi}, \quad (29)$$

where we have set $\sum_{k_{\hat{s}}=0}^{N-1} S_{k_{\hat{s}}}^z = 0$ and $S_0^z = (2n+1)\frac{1}{2}$ (and $2n+1$ being the number of pseudospin states in the direction \hat{s}) in the second line in order to obtain the third. Thus,

$$\{\mathcal{T}_{\hat{s}_\perp}, O_{ph}^{\hat{s}_\perp}\} = 0, \quad [H^{(*)}, \mathcal{T}_{\hat{s}_\perp}] = 0 = [H^{(*)}, O_{ph}^{\hat{s}_\perp}]. \quad (30)$$

These relations imply the existence of two degenerate states labelled by the center of mass angular position along \hat{s}_\perp ($\Theta_{\hat{s}_\perp}$)

$$|\Theta_{\hat{s}_\perp} = 0\rangle, \quad |\Theta_{\hat{s}_\perp} = \pi\rangle, \quad (31)$$

with transitions from one to the other taking place via the twist operator O_{ph}

$$O_{ph}^{\hat{s}_\perp} |\Theta_{\hat{s}_\perp} = 0\rangle = |\Theta_{\hat{s}_\perp} = \pi\rangle \quad (32)$$

We now unveil another two-fold degeneracy of the ground state manifold. By first defining pseudospin degrees of freedom along a given direction of momentum space (\hat{s}) that are resolved in terms of the eigenvalue of the helicity operator ($\eta = \pm 1$)

$$\tilde{S}_0^{\hat{s},z} = \sum_k \delta_{\eta_k, -1} S_{k, \eta_k}^{\hat{s},z}, \quad \tilde{S}_1^{\hat{s},z} = \sum_k \delta_{\eta_k, +1} S_{k, \eta_k}^{\hat{s},z} \quad (33)$$

we define a helicity twist operator $O_H^{\hat{s}}$

$$O_H^{\hat{s}} = e^{i\frac{2\pi}{2} (0 \cdot \tilde{S}_0^{\hat{s},z} + 1 \cdot \tilde{S}_1^{\hat{s},z})}. \quad (34)$$

Then, we define the helicity inversion operator \mathcal{T}_H

$$\mathcal{T}_H^{\hat{s}} \equiv e^{i\hat{H}_e^{\hat{s}}} : S_{k, \eta_k}^{\hat{s},z} \rightarrow S_{k, -\eta_k}^{\hat{s},z}, \quad (35)$$

where $\hat{H}_e^{\hat{s}}$ corresponds to the generator of helicity inversion of the center of mass along \hat{s} . These helicity twist

and translation operators follow the algebra

$$\begin{aligned} \mathcal{T}_H^{\hat{s}} O_H^{\hat{s}} \mathcal{T}_H^{\hat{s}\dagger} &= O_H^{\hat{s}} \times \exp \left[\frac{i2\pi}{2} \left(2\tilde{S}_0^{\hat{s},z} - [\tilde{S}_0^{\hat{s},z} + \tilde{S}_1^{\hat{s},z}] \right) \right] \\ &= O_H^{\hat{s}} \times \exp \left(i2\pi \tilde{S}_0^{\hat{s},z} \right), \\ &= O_H^{\hat{s}} \times e^{i2\pi(2n+1)\frac{1}{2}} = O_H^{\hat{s}} e^{i\pi}, \end{aligned} \quad (36)$$

where we have set $[\tilde{S}_0^{\hat{s},z} + \tilde{S}_1^{\hat{s},z}] = 0$ and $\tilde{S}_0^{\hat{s},z} = (2n+1)\frac{1}{2}$ in the second line in order to obtain the third. Thus,

$$\{\mathcal{T}_H^{\hat{s}}, O_H^{\hat{s}}\} = 0, \quad [H^{(*)}, \mathcal{T}_H^{\hat{s}}] = 0 = [H^{(*)}, O_H^{\hat{s}}]. \quad (37)$$

Again, these relation imply the existence of two degenerate states labelled by the eigenvalue of the generator of helicity inversion ($\hat{H}_e^{\hat{s}}$) of the center of mass along \hat{s}

$$|H_e^{\hat{s}} = 0\rangle, \quad |H_e^{\hat{s}} = \pi\rangle, \quad (38)$$

with transitions from one to the other taking place via the twist operator O_{ph}

$$\mathcal{T}_H^{\hat{s}} |H_e^{\hat{s}} = 0\rangle = |H_e^{\hat{s}} = \pi\rangle. \quad (39)$$

Importantly, we find that

$$\begin{aligned} [\mathcal{T}_H^{\hat{s}}, \mathcal{T}_{\hat{s}\perp}^{\hat{s}}] &= 0 = [O_H^{\hat{s}}, O_{ph}^{\hat{s}\perp}], \\ \{\mathcal{T}_H^{\hat{s}}, O_H^{\hat{s}}\} &= 0 = \{\mathcal{T}_{\hat{s}\perp}^{\hat{s}}, O_{ph}^{\hat{s}\perp}\}. \end{aligned} \quad (40)$$

Thus, these four operators together label the four-fold degenerate ground state manifold. As noted above, this matches the result for the phenomenological BF Chern-Simons gauge field theory formulation of Hansson et al.³⁸ Finally, the topological order is protected by the spectral gap

$$\Delta_{top} = E_{S^z=1} - E_{S^z=0} = \frac{V^*}{N^*} \quad (41)$$

separating the degenerate ground state manifold from the lowest lying excited state of the effective Hamiltonian H_{coll} (eq.(11)). Further, these ground states are also separated from the single-particle excitations by a many-body gap (Δ_{MB}) that arises from the helicity backscattering term, $(\bar{V}^*/N^*) \sum_k (S_k^+ S_{-k}^- + \text{h.c.})$, contained within the effective Hamiltonian H_{coll} (eq.(11))⁷⁰

$$\Delta_{MB} = \langle \psi_0 | \frac{\bar{V}^*}{N^*} \sum_k (S_k^+ S_{-k}^- + \text{h.c.}) | \psi_0 \rangle. \quad (42)$$

C. Spectral flow, plateau ground states and topological quantum numbers

As mentioned in the previous subsection, by tuning the ratio $\Phi \equiv \bar{\epsilon}^*/\bar{V}^*$, we can access ground states with different number of Cooper pair bound states (i.e., the eigenvalue of the operator S^z). We will now study the passage between these ground states, and also show the journey

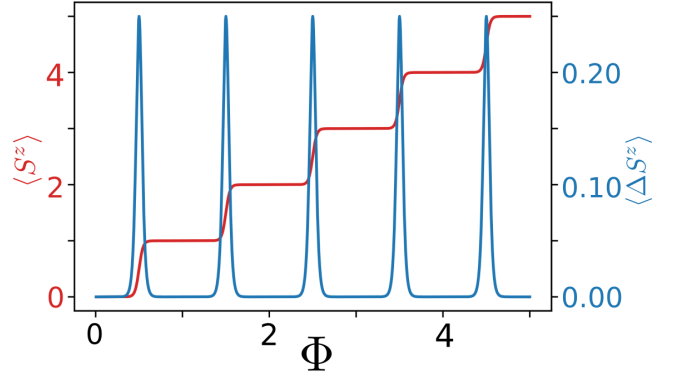


FIG. 4. Variation of $\langle S^z \rangle$ (red curve, and y-axis on left) and $\langle \Delta S^z \rangle$ (blue curve, and y-axis on right) with effective AB flux Φ at small temperature $T = 0.01$ (in units of k_B). $\langle S^z \rangle$ and $\langle \Delta S^z \rangle$ are computed using the effective CPI Hamiltonian eq.(11). See text for discussion.

towards a metallic (gapless) ground state (i.e., with a vanishing number of Cooper pair bound states).

We recall that for $\Phi = 0$, the ground state is given by $|\psi_g\rangle = |S = N^*/2, S^z = 0\rangle$, i.e., a state with N^* Cooper pairs. The action of S^+ on $|\psi_g\rangle$ is

$$\begin{aligned} S^+ \left| \frac{N^*}{2}, 0 \right\rangle &= \sqrt{(S - S^z)(S + S^z + 1)} \left| \frac{N^*}{2}, 1 \right\rangle \\ &= \sqrt{\frac{N^*}{2} \left(\frac{N^*}{2} + 1 \right)} \left| \frac{N^*}{2}, 1 \right\rangle, \end{aligned} \quad (43)$$

i.e., lowers the Cooper pair number by 1. Energetically, this is equivalent to a value of the parameter Φ in H_{coll} within the range $0.5 < \Phi < 1.5$. In the same way, $\frac{m}{2} < \Phi < \frac{m}{2} + 1$ ($m \in \mathcal{Z}$) leads to a ground state $|N^*/2, m\rangle$, such that for $\Phi > (N^* - 1)/2$, we attain a ground state with a vanishing number of Cooper pairs. This amounts to reducing the spectral gap of the CPI phase in a step-like manner, until a gapless spectrum (the “metal”) is attained. Thus, tuning the parameter Φ amounts to a process of spectral flow between various ground states. Each gapped ground state (corresponding to different values of S^z) possesses topological features (as discussed in the previous subsection).

At zero temperature, in the presence of a pairing-induced gap Δ , these gapped ground states will show plateaux in a variation of $\langle S^z \rangle$ with $\Phi = \bar{\epsilon}^*/\bar{V}^*$ (see Fig.4 for a small $k_B T = 0.04$). Further, it is easily seen that at various half-integer values of $\Phi = m + 1/2$, the ground state becomes degenerate via level-crossings, i.e., a linear combination of $|S = N^*/2, S^z = m\rangle$ and $|S = N^*/2, S^z = m + 1\rangle$

$$|\psi_{PT}^m\rangle = c_1 \left| \frac{N^*}{2}, m \right\rangle + c_2 \left| \frac{N^*}{2}, m + 1 \right\rangle, \quad (44)$$

where $|c_1|^2 + |c_2|^2 = 1$. As shown in Fig.4, these correspond to transitions between plateaux in $\langle S^z \rangle$ and lead to large fluctuations ($\langle \Delta S^z \rangle$) in S^z . It can be shown

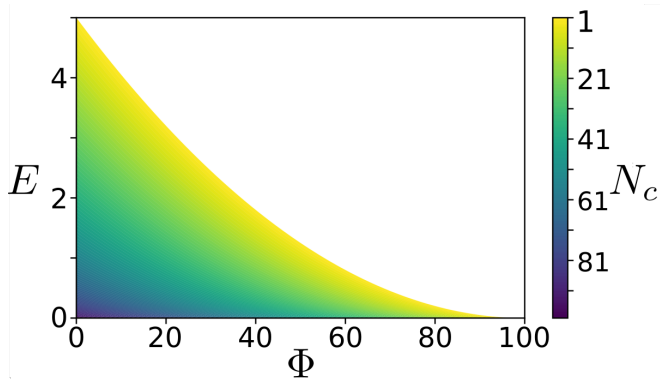


FIG. 5. Variation of the energy spectrum (E , y-axis) of the effective CPI Hamiltonian (eq.(11)) with the effective AB flux Φ (x-axis) for a system of 200 electrons. The colour scale represents the number of Cooper pairs (N_C). The bright yellow border represents the transition between the metal (white region) and CPI phases upon tuning Φ .

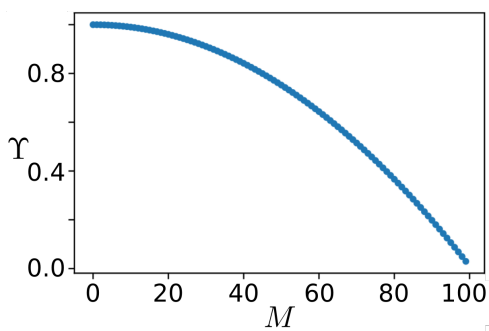


FIG. 6. Variation of the normalized helicity cross correlation (Υ) with the ground state eigenvalue of S_z (M) for a system of 200 electrons. M is increased by increasing the flux Φ . The large values of Υ for $M \rightarrow 0$ characterises the stable CPI phase, and the curve represents the passage to the metal ($\Upsilon \rightarrow 0$ as $M \rightarrow 100$).

that the largest $\langle \Delta S^z \rangle$ is obtained for $c_1 = 1/\sqrt{2} = c_2$. As noted above, the final level-crossing is attained at $\Phi = (N^* - 1)/2$. In Fig.5, we show a variation of the energy for excited states obtained from H_{coll} (computed with respect to the ground state energy) with the parameter Φ , and where the colour scale denotes the number (N_c) of Cooper pairs in a given state. The plot clearly shows the collapse of the excitation spectrum of the gapped plateaux as Φ is tuned towards passage from the final plateau into the gapless metal (white space in Fig.5).

This is reinforced by a study of the helicity cross correlation (Υ), i.e., inter-helicity two-particle scattering, defined as

$$\Upsilon = \langle S^+ S^- \rangle + \langle S^- S^+ \rangle - 2\langle S^+ \rangle \langle S^- \rangle, \quad (45)$$

where the expectation value is taken with respect to the ground state. For $|\psi_g\rangle = |S, S^z = M\rangle$, it can be shown that $\Upsilon = 2(S^2 + S - M^2)$. A plot of Υ versus M in

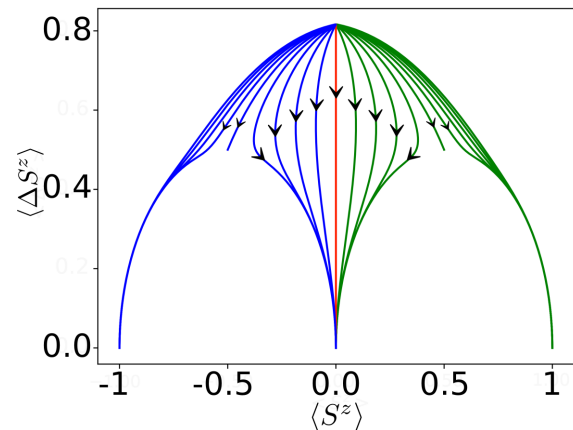


FIG. 7. Variation of $\langle S_z \rangle$ and $\langle \Delta S_z \rangle$ with lowering temperature (from $T = 1000$ to $T = 0$ (in units of k_B), and indicated through arrows) and flux $\Phi = 0$ towards the three CPI ground states $S_z = 0, \pm 1$ that are reached for the $S = 1$ system. $\langle S_z \rangle$ and $\langle \Delta S_z \rangle$ are computed using the CPI Hamiltonian (eq.(11)). See text for discussion.

Fig.6 shows that the strength of inter-helicity scattering gradually reduces as M increases, i.e., the parameter Φ is tuned towards the gapless metal.

Upon increasing the temperature, the plateaux are steadily degraded and the fluctuations $\langle \Delta S^z \rangle$ at the transitions increase in strength (Fig.4). In Fig.7, we show a plot of $\langle \Delta S^z \rangle$ against $\langle S^z \rangle$ obtained from H_{coll} for different values of the parameter Φ and temperature T for the case of $S = 1, S^z = 0, \pm 1$. The blue curves are for $-1 \leq \Phi < 0$ (with $-1 \leq \langle S^z \rangle < 0$) and the green curves are for $0 < \Phi \leq 1$ (with $0 < \langle S^z \rangle \leq 1$). The direction of the arrows denote the lowering of temperature. Fig.7 shows that lowering T generically leads to a plateau ground state ($\langle S^z \rangle = 0, \pm 1, \langle \Delta S^z \rangle = 0$). On the other hand, there also exist special cases when lowering T leads to (unstable) ground states located precisely at the plateau transitions ($\langle S^z \rangle = 1/2 = \pm \langle \Delta S^z \rangle$). While the figure shows the numerical computation for H_{coll} with $S = 1$, we have observed that a similar plot for a much larger value of S also shows the same ‘‘dome’’-like structure of the curves.

IV. ENTANGLEMENT FEATURES OF CPI

A. Entanglement Spectrum

We begin our discussion of the entanglement features of the CPI phase with an investigation of the entanglement spectrum for the plateau ground states, whose wavefunction is given by $|\psi_P\rangle = |S, S_z\rangle$ for $\Phi = m, m \in \mathcal{Z}$. We will also present the entanglement spectrum at the plateau transitions where the ground state is degenerate, $\psi_{PT} = \frac{1}{\sqrt{2}}(|S, S_z\rangle + |S, S_z + 1\rangle)$ for $\Phi = m/2, m \in \mathcal{Z}$. We first Schmidt decompose the state $|\psi_P\rangle$ (with $n =$

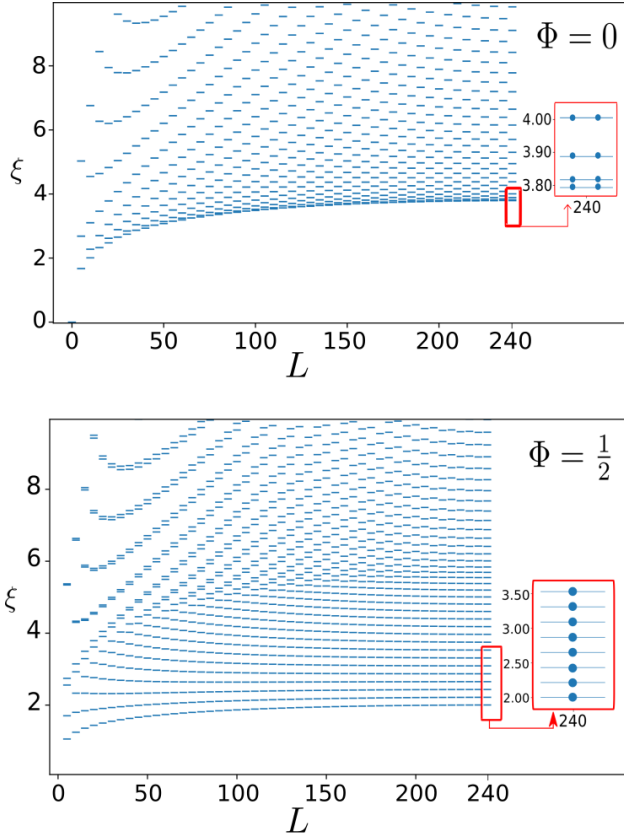


FIG. 8. Entanglement spectrum (ES, $\xi_i = -\log_2 \lambda_i$) of a subsystem of size L in the ground state wavefunction at $\Phi = 0$ (eq.(14), upper plot) and at $\Phi = 1/2$ (eq.(44), lower plot) for a system of $N^* = 488$ Cooper pairs and as a function of the subsystem size L . The index i labels the ES eigenvalues. The upper inset shows the double degeneracy for all levels, while the lower inset shows that the degeneracy is lifted at $\Phi = 1/2$.

$S^z + N^*/2$ \uparrow -pseudospins) into subsystems of length L and $N^* - L$ (with l and $n - l$ \uparrow -pseudospins respectively)

$$|\psi_P\rangle = \sum_{l=l_{min}}^{l_{max}} \lambda_l^n |L, l\rangle \otimes |N^* - L, n - l\rangle, \quad (46)$$

where λ_l^n are the Schmidt coefficients. The number l ranges within l_{min} and l_{max} given by

$$l_{max} = n \text{ for } n \leq L \text{ and} \quad (47)$$

$$= L \text{ for } n > L, \quad (48)$$

$$l_{min} = 0 \text{ for } n \leq (N^* - L) \text{ and} \quad (49)$$

$$= n - (N^* - L) \text{ for } n > (N^* - L). \quad (50)$$

From the pure state density matrix $\rho_P = |\psi_P\rangle\langle\psi_P|$, we can then obtain a reduced density matrix $\rho_{P,L}(n)$ for a subsystem of L pseudospins

$$\rho_{P,L}(n) = \sum_{l=l_{min}}^{l_{max}} (\lambda_l^n)^2 |L, l\rangle\langle L, l|. \quad (51)$$

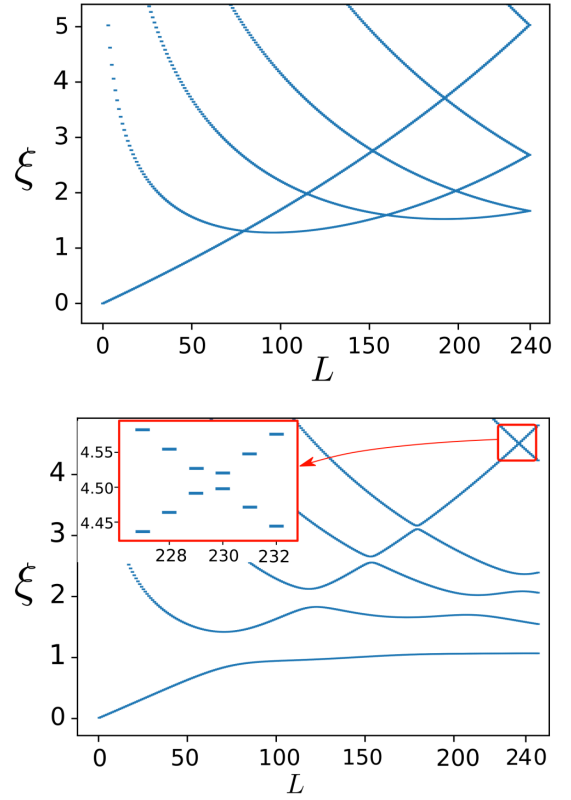


FIG. 9. Entanglement spectrum (ES, $\xi_i = -\log_2 \lambda_i$) of a subsystem of size L in the ground state wavefunction at $\Phi = 240$ (eq.(14), upper plot) and at $\Phi = 240.5$ (eq.(44), lower plot) for a system of $N^* = 488$ Cooper pairs and as a function of the subsystem size L . The index i labels the ES eigenvalues. The inset in the lower figure shows the lifting of degeneracies observed in the upper plot.

The Schmidt coefficients (λ_l^n) are determined by the combinatorial factor that specifies the number of ways one can choose l \uparrow spins from n \uparrow spins:

$$(\lambda_l^n)^2 = \frac{C_l^L C_{n-l}^{N^*-L}}{C_n^{N^*}} = \frac{L!(N^* - L)!n!(N^* - n)!}{l!(L - l)!(n - l)!(N^* - L - n + l)!N^*!}. \quad (52)$$

At the plateau transitions, we start with a pure state density matrix obtained from the linear superposition state $|\psi_{PT}\rangle$, $\rho_{PT} = |\psi_{PT}\rangle\langle\psi_{PT}|$, and proceed identically as above to obtain the reduced density matrix $\rho_{PT,L}(n)$. The entanglement spectrum (ES) is obtained from the Schmidt eigenvalues, $\xi_i^n = -\log_2(\lambda_i^n)$, for $\rho_{P,L}(n)$ and $\rho_{PT,L}(n)$ with given values of N^* and L .

For a fixed $N^* = 488$ pseudospins, we plot the ES for various values of the reduced partition size L for the case of the plateau at strong coupling $\Phi = 0$ and the first plateau transition at $\Phi = 1/2$ in Fig.8(a) and (b) respectively. The double degeneracy of all levels in the ES for all L at $\Phi = 0$ is revealed by the small splitting revealed at $\Phi = 1/2$. This double degeneracy for the *entire spectrum* reflects the additional particle-hole symmetric na-

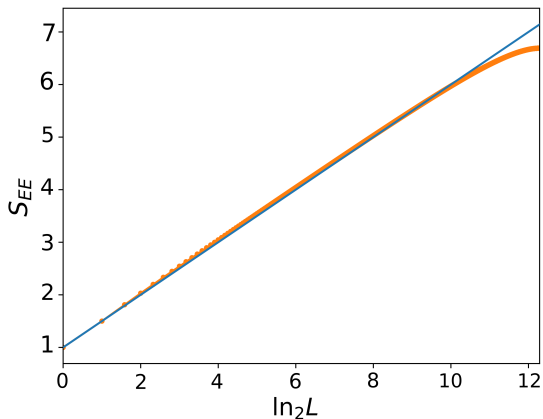


FIG. 10. The red curve shows the variation of the entanglement entropy (EE) with $\ln_2(L)$ (L is the subsystem size) for the CPI ground state at $\Phi = 0$ for a system of $N^* = 488$ Cooper pairs. The blue curve is a linear fit to the form $1/2 \ln_2(L) + 1$. See text for discussion.

ture of the CPI ground state at $\Phi = 0$, and corroborated by the degeneracy lifting precisely at the transition point ($\Phi = 1/2$). We have checked that a similar degeneracy of the ES is revealed for all other plateau ground states at $\Phi = m$, $m \in \mathcal{Z}, m > 0$ for *only* a bi-partitioning of the system $L = N^*/2$. For instance, in Fig.9, we present the ES at a weak coupling plateau $\Phi = 240$ and plateau transition $\Phi = 240.5$ for a system of $N^* = 488$ pseudospins. Here too, the plots clearly show the double degeneracy of the plateau and the degeneracy lifting at the transition. The restricted degeneracy of the ES for all bi-partitioned CPI plateaux ground states with $\Phi > 0$ may be associated with their topological order. However, this requires further investigation.

B. Entanglement Entropy of the plateau ground states and transitions

We now compute the bipartite entanglement entropy in momentum space for various plateau ground states obtained by tuning the parameter ϕ . As before, we take a system where N^* and L are the total number of pseudospins and number of pseudospins within the reduced subsystem, while n and l are the number of \uparrow -pseudospins within N^* and L respectively. The bipartite entanglement entropy (S_{EE}) can simply from the Schmidt coefficients (λ_l^n) via the following formula

$$S_{EE}(n, L) = - \sum_{l=l_{min}}^{l_{max}} d_l |\lambda_l^n(L)|^2 \log_2 |\lambda_l^n(L)|^2, \quad (53)$$

where d_l is the degeneracy factor for the l th state of the entanglement spectrum. We have observed earlier in Fig.8(a) that for the case of the strong coupling ground state at $\Phi = 0$, $d_l = 2 \forall l$ due to the two topologically

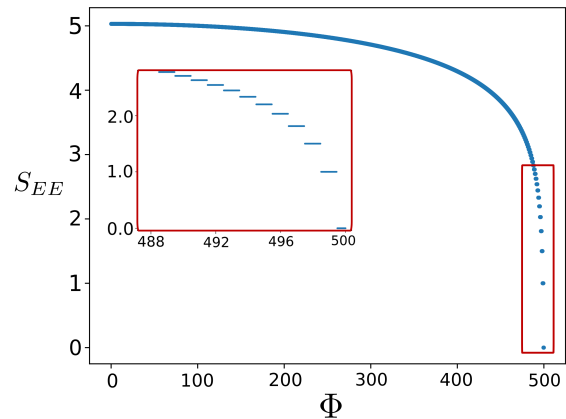


FIG. 11. Plot of bipartite entanglement entropy for various CPI ground states corresponding to different various flux Φ of a system of $N^* = 500$ Cooper pairs. Inset shows the rapid fall of the bipartite EE upon approaching the CPI to Metal ($\Phi = 500$) transition.

distinct sectors $X = \pm 1$. The appearance of the constant $d_l = 2$ thus signifies the influence of the topological nature of the ground state manifold on S_{EE} . In Fig.10, we see that S_{EE} varies linearly with $\log_2(L)$ for $N^* = 10000$ for a large range of L , departing from the linear variation only very near the equipartitioning value of $L = N^*/2$. We have found the value of the slope to be a simple number ($1/2$) as Φ is varied through the first 2000 plateaux. However, it is not clear whether this indicates a universality of plateaux ground states observed at strong coupling with those at intermediate coupling. Unlike the observation of logarithmic scaling of S_{EE} with subsystem size in 1+1D quantum critical systems (see Ref.⁷¹ and references therein), the log-scaling observed by us in Fig.10 is indicative of the physics of a gapped ground state of the effectively zero-dimensional Hamiltonian H_{coll} (eq.(11)) obtained from the RG⁷².

The value of the intercept (1, in units of $\log_2(2)$) is the entanglement entropy of a subsystem size of $L = 1$ and corresponds to a maximally mixed pseudospin. The intercept is, however, observed to decrease steadily beyond the first 200 plateaux as Φ is varied, indicating that a single pseudospin's entanglement with the rest of the system within a plateau ground state is lowered as Φ is tuned towards weak coupling. Further, in Fig.11, we present the variation of the bipartite S_{EE} with the parameter Φ for a system with $N^* = 1000 = 2L$. The plot clearly shows that the $\Phi = 0$ plateau possesses the largest entanglement content, and that this is rapidly lowered to zero as Φ is tuned through various plateaux towards the gapless metal⁷².

In contrast to Fig.10 above, the entanglement entropy at the first transition ($\Phi = 0.5$, see Fig.12) computed using eq.(44) for $c_1 = 1/\sqrt{2} = c_2$ for various system sizes N^* displays a non-monotonic variation of S_{EE} with the subsystem size L . Remarkably, S_{EE} displays a com-

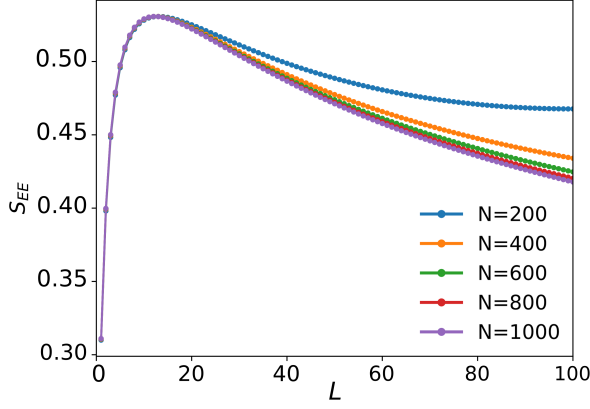


FIG. 12. Variation of the entanglement entropy (S_{EE}) with subsystem size L at the first plateau transition ($\Phi = 0.5$) for various system sizes in the range $100 \leq N^* \leq 1000$ Cooper pairs.

mon peak at $L^* = 7$ for system sizes ranging between $100 \leq N^* \leq 1000$, with all the curves collapsing onto a universal curve for $L \leq L^*$. This suggests that the entanglement content at the first plateau transition is dominated by small subsystem size. While the last data point in Fig.12 corresponds to the equipartition $S_{EE}(L = N^*/2)$ for $N^* = 100$, we have checked that $S_{EE}(L = N^*/2)$ falls logarithmically with N^* . As shown in Fig.13, we have also observed that the maximum value of S_{EE} observed in Fig.12 remains unchanged (as Φ is tuned across various plateau transitions for a system of size $N^* = 1000$) until almost the very last few transitions, where it falls rapidly to zero. On the other hand, L^* increases gradually with Φ , climbing rapidly at the last few transitions. This clearly demonstrates that the peak in S_{EE} is a universal feature of the plateau transitions. We have also observed that the S_{EE} for a single pseudospin (i.e., $L = 1$) falls to zero gradually from its value at the first transition as Φ is varied.

Finally, we present the computation of the entanglement entropy of the plateau ground states and transitions at finite temperature. The thermal density matrix for the plateau ground state $|N^* = 2S, n = S^z + \frac{N^*}{2}\rangle$ can be written as

$$\rho(\beta) = \sum_n \frac{e^{-\beta E_n}}{Z} |N^*, n\rangle \langle N^*, n|, \quad (54)$$

where β is the inverse temperature and Z the partition function. Equipartitioning the system precisely as described earlier in eqs.(51)-(52) (with $L = N^*/2$), we obtain the thermal reduced density matrix as

$$\rho_L(\beta) = \sum_{l,n} \frac{e^{-\beta E_n}}{Z} (\lambda_l^n)^2 |L, l\rangle \langle L, l|. \quad (55)$$

The reduced density matrix is easily seen to be diagonal

$$[\rho_L(\beta)]_{l,l'} = \delta_{l,l'} \sum_n (\lambda_l^n)^2 \frac{e^{-\beta E_n}}{Z}, \quad (56)$$

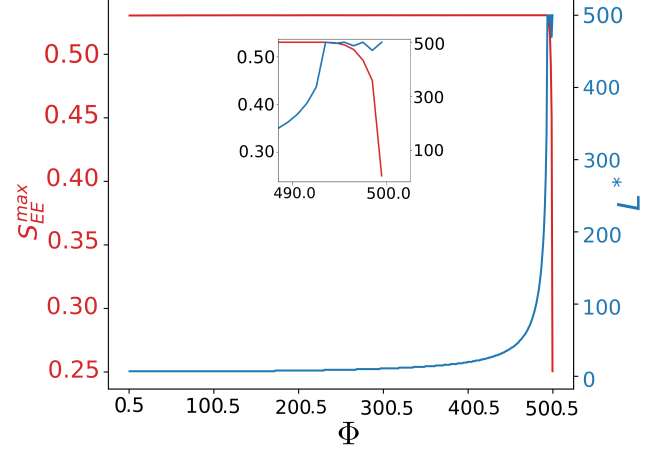


FIG. 13. Plot of the maximum entanglement entropy (S_{EE}^{max} , red curve, left y-axis) and the corresponding subsystem size (L^* , blue curve, right y-axis) at the transitions between various CPI ground states as Φ is varied for a system of $N_C = 500$ Cooper pairs. Inset: Rapid variation of S_{EE}^{max} and L^* with Φ upon approaching the CPI to Metal ($\Phi = 500$) transition.

such that the entanglement entropy at a non-zero temperature is obtained as

$$S_{EE}(L, \beta) = - \sum_l [\rho_L(\beta)]_{l,l} \log_2([\rho_L(\beta)]_{l,l}). \quad (57)$$

Precisely the same formalism can also be carried out with the state equal admixture state at the plateau transition ($|\psi\rangle_{PT}$).

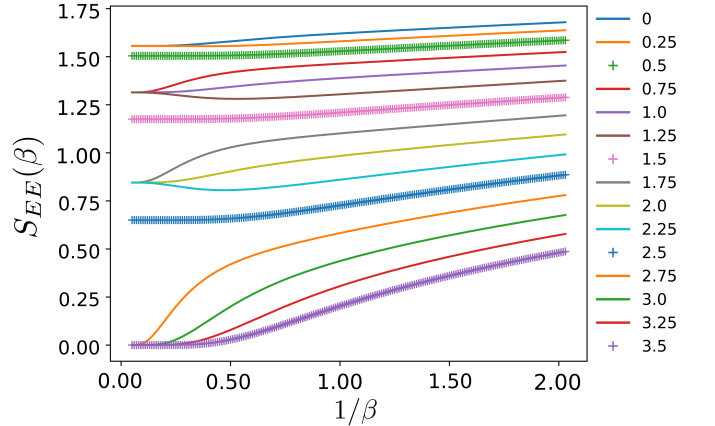


FIG. 14. Variation of the equipartition entanglement entropy ($S_{EE}(\beta)$) with temperature (β^{-1}) for a subsystem size $L = 4$ Cooper pairs. Various coloured curves correspond to the CPI ground states and transition ground states at different values of the flux Φ . See text for discussion.

In Fig.14, we present a numerical evaluation of $S_{EE}(L, \beta)$ for a subsystem of $L = 4$ pseudospins with varying $k_B T = \beta^{-1}$ for the first four plateaus (coloured curves centered about $\Phi = 0, 1, 2$ and 3) and transitions (+

symbol curves centered about $\Phi = 0.5, 1.5, 2.5$ and 3.5). While we have chosen a small system here ($N^* = 8$) for the sake of visual clarity, we have checked that all features of the plot are qualitatively unchanged for larger N^* . Remarkably, the plot shows that the S_{EE} corresponding to the transitions clearly separates all curves arising from neighbouring plateaus for temperatures $k_B T \ll V^*$. The S_{EE} curves for all Φ corresponding to a plateau collapse to a universal value at $T = 0$ characteristic of that plateau. Thermal fluctuations are observed to affect the curves of both the plateaus and the transitions in the same manner. For instance, the position of the divergence of the curves for a given plateau as T is increased suggests the robustness of that plateau to thermal transitions. Clearly, the $\Phi = 0$ plateau (strong coupling) is the most robust, the $\Phi = 1$ slightly less and so on, ending at the last plateau (at $S_{EE}(T = 0) = 0$) beyond which lies the gapless metal. Similarly, the curves for transitions associated with higher plateaus depart from their initial flat behaviour at lower temperatures in comparison to that for lower plateaus. The domination of thermal fluctuations as T is raised is also clearly observed: various S_{EE} curves corresponding to a particular $T = 0$ plateau show a linear increase with T asymptotically, and with a slope common to that of the S_{EE} curve for the transition that leads to the next plateau (e.g., the slopes of the S_{EE} curves for $\Phi = 0, 0.25$ and 0.5 are the same for large T etc.).

V. PASSAGE TO THE BCS GROUND STATE

In order to chart the passage from the number-fixed CPI ground state to the conjugate phase-fixed BCS ground state, we will carry out the RG analysis upon adding a global $U(1)$ -symmetry breaking term ($-2B \sum_k S_k^x$, $B > 0$) to the collective Hamiltonian H_{coll} (eq.(9)) with the repulsive density-density interaction $U = 0$. The B field represents a Josephson coupling to an external phase-fixed BCS superconductor. We will show that at large B , the RG flow leads to a BCS-like ground state. This will also be reinforced by studying the variation of several quantities with the symmetry-breaking field B , e.g., inter- k entanglement, helicity-partitioned entanglement, helicity cross-correlation, pair number fluctuation etc. Thus, we begin with the Hamiltonian

$$H_{SB} = -\frac{2\bar{\epsilon}}{N} \sum_k S_k^z - \frac{\bar{V}}{2N} \sum_{kk'} (S_k^+ S_{k'}^- + \text{h.c.}) - 2|B| \sum_k S_k^x \quad (58)$$

The RG equations for $\bar{\epsilon}$ and \bar{V} are those given earlier in eq.(8) (with $\bar{W} = \bar{V}/N$), while the RG for the symmetry-breaking field B is found to be

$$\frac{\Delta|B^{(j)}|}{\Delta \log \frac{\Lambda_j}{\Lambda_0}} = -\frac{1}{2} \frac{|\bar{W}^{(j)}||B^{(j)}|}{\left(\omega - \frac{\epsilon^{(j)}}{2} - \frac{U}{4}\right)}. \quad (59)$$

In the regime $\omega < \frac{\epsilon^{(j)}}{2} + \frac{U}{4}$, both \bar{W} and B are found to be RG relevant. From the RG eqs.(8) and (59), we find

$$\frac{\Delta(\epsilon)}{\Delta|\bar{W}|} = -1, \quad \frac{\Delta(\epsilon)}{\Delta B} = -\frac{|\bar{W}|}{2B} \Rightarrow \frac{\Delta|\bar{W}|}{\Delta B} = \frac{|\bar{W}|}{2B}, \quad (60)$$

indicating that while both $|\bar{W}|$ and B grow to strong coupling under the RG flow, the ratio $|\bar{W}|/B$ remains invariant. This shows that while the original BCS mean-field Hamiltonian² is achieved only in the limit of the RG invariant $|\bar{W}|/B \rightarrow 0$, a $U(1)$ -symmetry broken BCS-like effective Hamiltonian is emergent from the RG flow at strong coupling

$$H_{SB} = H_{coll} - B^* S_x, \quad (61)$$

where H_{coll} is given in eq.(10). Further, in appendix B, we show that the familiar form of an exponentially small spectral gap is obtained from the RG flow to strong coupling in B . In considering the effective Hamiltonian obtained from the RG, we will henceforth drop the $*$ symbol from all couplings. Clearly, as $[S^z, H_{SB}] \neq 0$, the total Cooper pair number operator (proportional to S^z) is no longer a conserved quantity. Further, the topological order parameter Z encountered earlier is no longer a good order parameter, as $[Z, H_{SB}] \neq 0$: the effective Hamiltonians $H_{coll} \equiv H_{SB}(B = 0)$ and $H_{SB}(B \neq 0)$ are topologically inequivalent. We will demonstrate below that, as B is tuned to larger values, the Cooper pair number fluctuations increase rapidly while the fluctuations in the conjugate $U(1)$ global phase is lowered. This indicates that a BCS-like ground state is attained under the RG flow of B to strong coupling.

In commonality with the BCS ground state, the ground state wavefunction for H_{SB} is given by a linear superposition of states with different S^z (eq.(14))

$$\begin{aligned} |\psi(B)\rangle &= \sum_{S^z=-S}^S \alpha_B(S^z) |S, S^z\rangle \\ &= \sum_{S^z=-S}^S \alpha_B(S^z) \left(\sum_k c_{k\uparrow}^\dagger c_{-k\downarrow}^\dagger \right)^{S-S^z} |vac\rangle \quad (62) \end{aligned}$$

where the (normalised) coefficients $\alpha_B(S^z)$ are functions of the symmetry-breaking field B . We will also show below that several properties of $|\psi(B)\rangle$ closely resemble those of $|\psi_{BCS}\rangle$ as B is tuned to large values. For instance, we will show that at large B , $|\psi(B)\rangle$ leads to vanishing inter- k entanglement. We recall that a vanishing inter- k entanglement entropy is a special property of the BCS ground state, arising from the fact that different k -momenta electron-pair states are decoupled from one another.

A. Properties of the ground state

In order to obtain various properties of the ground state of the effective Hamiltonian H_{SB} , we carry out exact

diagonalization computations for system sizes of $N^* = 50$ Cooper pairs. We compute various quantities related to the ground state, e.g., fluctuation in the Cooper pair number and the conjugate global phase, helicity cross correlations, various measures of entanglement etc.

In Fig.15, we present the variation of the fluctuations in the Cooper pair number ($\langle \Delta N \rangle \equiv \langle \Delta S^z \rangle$, blue curve) and conjugate global phase ($\langle \Delta \phi \rangle$, red curve). The plot clearly shows the rapid decline in $\langle \Delta \phi \rangle$ as B is increased, together with an equally rapid growth in $\langle \Delta N \rangle$. We have also observed that a plot of the number fluctuations $\langle \Delta S^z \rangle$ versus $\langle S^z \rangle$ for different values of Φ and B is strikingly similar to Fig.7. Further, we shall see below that the entanglement content of the fluctuations induced by a non-zero B are very different from that induced by thermal fluctuations.

The red curve in Fig.16 shows the variation of the helicity cross correlations (Υ , eq.(45)) with B . The plot displays the rapid decline of Υ that is characteristic of the CPI ground state towards zero as B is tuned to large values. This is expected, as Υ vanishes for the BCS ground state. The blue curve in Fig.16 shows the variation of the helicity-partitioned entangled entropy (Ξ) with B . Ξ is derived from the reduced density matrix obtained by tracing out one of the two helicities ($\eta_{\pm} = \text{sgn}(k)\text{sgn}(\sigma) = \pm 1$). The helicity-partitioned ground state wavefunction can be written as follows

$$|\psi_g(B)\rangle = \sum_{m=-S}^S C_m(B) |S, S^z = m\rangle, \\ |S, m\rangle = \sum_{m_{\eta_+}, m_{\eta_-}} D_{m_{\eta_+}, m_{\eta_-}}^m |S/2, m_{\eta_+}; S/2, m_{\eta_-}\rangle \quad (63)$$

where D_n^m 's are Clebsch-Gordon coefficients given by

$$D_{m_{\eta_+}, m_{\eta_-}}^m = \delta_{m, m_{\eta_+} + m_{\eta_-}} \times \\ \sqrt{\frac{(S!)^2 (S+m)! (S-m)!}{(2S)! (\frac{S}{2} - m_{\eta_+})! (\frac{S}{2} + m_{\eta_+})! (\frac{S}{2} - m_{\eta_-})! (\frac{S}{2} + m_{\eta_-})!}} \quad (64)$$

In the ground state, the total spin (S) is maximised, ensuring that the total spin within each helicity sector is also maximised (and taken to be $S/2$). By tracing over a certain helicity (η_+), we obtain a reduced density matrix $\rho_{\eta_-} = \text{Tr}_{\eta_+} |\psi_g(B)\rangle \langle \psi_g(B)|$. The set of eigenvalues ($\{\lambda_i\}$) obtained by diagonalising ρ_{η_-} then gives the helicity-partitioned entanglement entropy Ξ (i.e., a measure of the entanglement between the opposite helicities)

$$\Xi(B) = - \sum_i \lambda_i(B) \log_2(\lambda_i(B)). \quad (65)$$

The variation of this entanglement entropy with B is shown via the blue curve in Fig.16, displaying a rapid decline towards zero in the entanglement between the helicities η_+ and η_- as B is tuned to large values. This is consistent with the fact that the BCS ground state does not possess helicity entanglement; this arises simply from the fact that the BCS ground state wavefunction

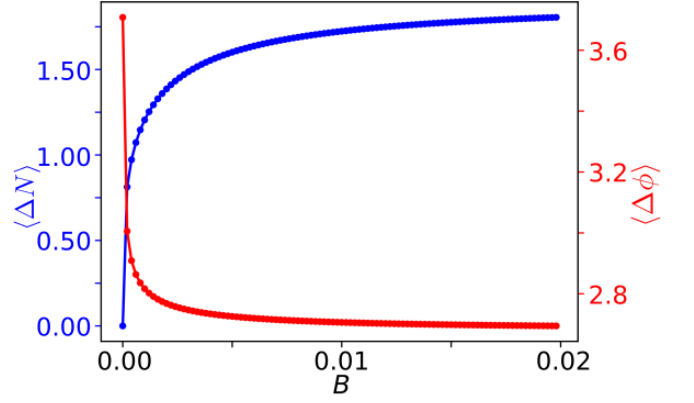


FIG. 15. Variation of fluctuation in number of Cooper pairs ($\langle \Delta N \rangle$, blue curve, left y-axis) and global phase ($\langle \Delta \phi \rangle$, red curve, right y-axis) with the global $U(1)$ symmetry breaking field B for a system of $N^* = 50$ Cooper pairs.

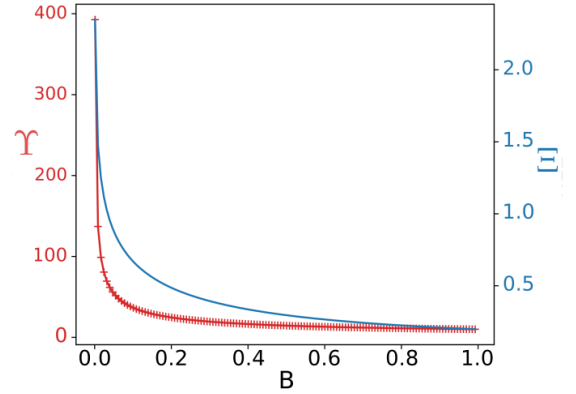


FIG. 16. Variation of helicity cross correlations (Υ , red curve, left y-axis) and helicity partitioned entanglement entropy (Ξ , blue curve, right y-axis) in number of Cooper pairs ($\langle \Delta N \rangle$, blue curve, left y-axis) with the global $U(1)$ symmetry breaking field B for a system of $N^* = 50$ Cooper pairs.

is a direct product state of pairs of electronic momenta ($k, -k$).

On the other hand, as Cooper pairs in the s-wave BCS state are spin singlets, there is a non-zero entanglement between the two spins of a Cooper pair⁴. Thus, in order to distinguish the CPI and BCS ground states further, we compute the entanglement entropies S_{EE}^k and S_{EE}^S by partitioning the ground state $|\psi_g(B)\rangle$ for an analytically tractable system of two Cooper pairs ($(k_1 \uparrow, -k_1 \downarrow)$ and $(k_2 \uparrow, -k_2 \downarrow)$) in the momentum variable (k_1, k_2) and the spin variable (\uparrow, \downarrow) respectively for the case of $\bar{\epsilon} = 0$ (strong coupling limit) in the Hamiltonian H_{coll} (eq.(10)). For this system of two coupled pseudospins, $S = 1$ and the ground state wavefunction is

$$|\psi_g(B)\rangle = \sum_{\alpha=-1}^1 C_\alpha(B) |S = 1, S^z = \alpha\rangle, \quad (66)$$

where the coefficients C_α are a function of the field B

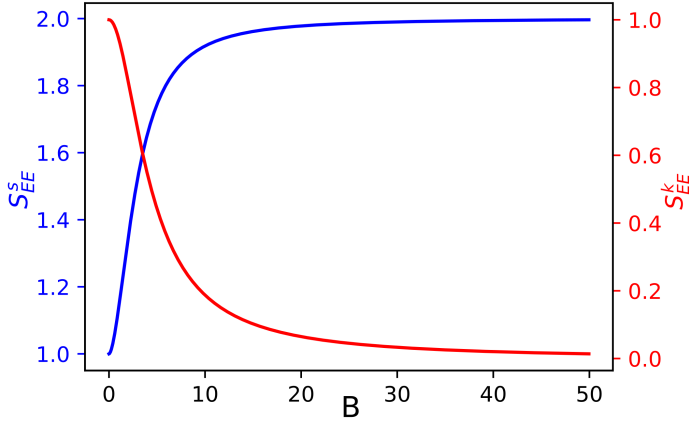


FIG. 17. Variation of spin partitioned entanglement entropy (S_{EE}^S , blue curve, left y-axis) and momentum partitioned entanglement entropy (S_{EE}^k , red curve, right y-axis) with the global $U(1)$ symmetry breaking field B for a prototypical system of $N^* = 2$ Cooper pairs.

and the coupling V/N given by

$$\{C_\alpha\} = \mathcal{N} \left(1, -\frac{\alpha + \sqrt{\alpha^2 + 8\beta^2}}{2\beta}, 1 \right) \xrightarrow{\beta \gg 1} \left(\frac{1}{2}, -\frac{1}{\sqrt{2}}, \frac{1}{2} \right), \quad (67)$$

where \mathcal{N} is the normalisation factor, $\alpha = \frac{V}{N}$ and $\beta = \frac{B}{\sqrt{2}}$. By writing the states $|S, S^z\rangle$ in the basis of $|n_{k\uparrow}n_{-k\downarrow}\rangle \otimes |n_{k'\uparrow}n_{-k'\downarrow}\rangle$, i.e., the states $\{|0_\uparrow 0_\downarrow\rangle_k \otimes |0_\uparrow 0_\downarrow\rangle_{k'}, |0_\uparrow 0_\downarrow\rangle_k \otimes |1_\uparrow 1_\downarrow\rangle_{k'}, |1_\uparrow 1_\downarrow\rangle_k \otimes |0_\uparrow 0_\downarrow\rangle_{k'}, |1_\uparrow 1_\downarrow\rangle_k \otimes |1_\uparrow 1_\downarrow\rangle_{k'}\}$, the density matrix $\rho(B) = |\Psi_g(B)\rangle\langle\Psi_g(B)|$ is found to be

$$\rho(B) = \begin{bmatrix} |C_1|^2 & \frac{C_0 C_1}{\sqrt{2}} & \frac{C_0 C_1}{\sqrt{2}} & C_1 C_{-1} \\ \frac{C_0 C_1}{\sqrt{2}} & \frac{|C_0|^2}{2} & \frac{|C_0|^2}{2} & \frac{C_0 C_{-1}}{\sqrt{2}} \\ \frac{C_0 C_1}{\sqrt{2}} & \frac{|C_0|^2}{2} & \frac{|C_0|^2}{2} & \frac{C_0 C_{-1}}{\sqrt{2}} \\ C_1 C_{-1} & \frac{C_0 C_{-1}}{\sqrt{2}} & \frac{C_0 C_{-1}}{\sqrt{2}} & |C_{-1}|^2 \end{bmatrix}. \quad (68)$$

The momentum-partitioned reduced density matrix is then obtained by tracing out the k' pseudo-spin from the density matrix (68). The reduced density matrix ρ^k is written in the basis $\{|0_\uparrow 0_\downarrow\rangle_k, |1_\uparrow 1_\downarrow\rangle_k\}$

$$\begin{aligned} \rho^k &= \text{Tr}_{k'} \rho(B) \\ &= \begin{bmatrix} |C_1|^2 + \frac{C_0^2}{2} & \frac{C_0 C_1}{\sqrt{2}} + \frac{C_0 C_{-1}}{2} \\ \frac{C_0 C_1}{\sqrt{2}} + \frac{C_0 C_{-1}}{2} & |C_{-1}|^2 + \frac{C_0^2}{2} \end{bmatrix} \end{aligned} \quad (69)$$

The inter- k entanglement is S_{EE}^k calculated from the density matrix ρ^k . As shown via the red curve in Fig.17, S_{EE}^k reduces monotonically from its largest value at $B = 0$ as B is increased, displaying the destruction of the inter- k entanglement of the CPI ground state in the passage towards the BCS ground state.

Similarly, for the spin-partitioned entanglement entropy, we trace out a given spin sector, say \downarrow . Then, the reduced density matrix in the basis

$\{|0_k 0_{k'}\rangle_\uparrow, |0_k 1_{k'}\rangle_\uparrow, |1_k 0_{k'}\rangle_\uparrow, |1_k 1_{k'}\rangle_\uparrow\}$ is

$$\begin{aligned} \rho^\uparrow &= \text{Tr}_\downarrow \rho(B) \\ &= \begin{bmatrix} |C_1|^2 & 0 & 0 & 0 \\ 0 & \frac{|C_0|^2}{2} & 0 & 0 \\ 0 & 0 & \frac{|C_0|^2}{2} & 0 \\ 0 & 0 & 0 & |C_{-1}|^2 \end{bmatrix} \end{aligned} \quad (70)$$

The spin-partitioned entanglement entropy S_{EE}^k is obtained from ρ^\uparrow . As shown via the blue curve in Fig.17, S_{EE}^k increases steadily from its smallest value at $B = 0$ as B is increased, and saturates as $B \gg 1$. This shows the growth of the inter-spin entanglement of the BCS ground state in the passage from the CPI ground state. The limiting values of S_{EE}^k at $B = 0$ and $B \gg 1$ observed in Fig.17 can be understood as follows. At $B = 0$, we get $C_0 = 1$, $C_{-1} = C_1 = 0$, giving S_{EE}^k for the CPI ground state as $\log_2 2 = 1$, as seen in Fig.17. Similarly, the diagonal elements of the diagonal density matrix (71) at large B become $(\frac{1}{4}, \frac{1}{4}, \frac{1}{4}, \frac{1}{4})$. This shows that $\rho^\uparrow(B \gg 1)$ becomes maximally mixed in nature, leading to $S_{EE}^k(B \gg 1)$ saturating to the value seen in Fig.17

$$S = -4 \times \frac{1}{4} \log_2 \frac{1}{4} = 2 \log_2 2 = 2. \quad (71)$$

This is a clear signature of the maximal entanglement of the Cooper pair singlets in the BCS ground state.

Another diagnostic of the difference between the ground states at $B = 0$ and $B \gg 1$ lies in the occupation for the k -momentum electron

$$\langle n_k \rangle = \text{Tr}(\hat{n}_k \rho^\uparrow) = \frac{|C_0|^2}{2} + |C_{-1}|^2. \quad (72)$$

While at $B = 0$, $\langle n_k \rangle \equiv \langle n_k \rangle(\alpha, \beta)$, $\langle n_k \rangle \rightarrow 1/2$ as $B \gg 1$. Given that $\langle n_k \rangle$ follows the Fermi-Dirac distribution for the BCS ground state⁴, the result of $\langle n_k \rangle = 1/2$ obtained at $B \gg 1$ indicates that the collective Hamiltonian H_{SB} (eq.(61)) in the presence of a large $U(1)$ symmetry breaking coupling B describes the BCS superconductor near the Fermi surface.

We now present the entanglement entropy (S_{EE}) computed from partitioning the ground state $|\psi_g\rangle$ (with spin S) of Hamiltonian H_{SB} into two equal subsystems A and B such that $S = S_A + S_B$, $S_A = S/2 = S_B$ using the strategy adopted in eqs.(46)-(53). In Fig.18, we present a variation of S_{EE} with B computed for a system of 8 pseudospins, and for ground states of $H_{SB}(B = 0) \equiv H_{coll}$ at various values of $\Phi = \epsilon/V$. The plot shows the monotonic decrease for S_{EE} with B for all ground states with a non-zero number of Cooper pairs ($0 \leq \Phi < 4$), while the S_{EE} computed for the gapless ground state at $\Phi = 4$ shows a non-monotonic variation with B . The latter case corresponds to the entanglement related to superconducting phase fluctuations in a mean-field BCS Hamiltonian, i.e., a Hamiltonian H_{SB} in which the BS^x term induces pairing in the gapless spectrum of H_{coll} . While the BCS ground state corresponding to a vanishingly small S_{EE}

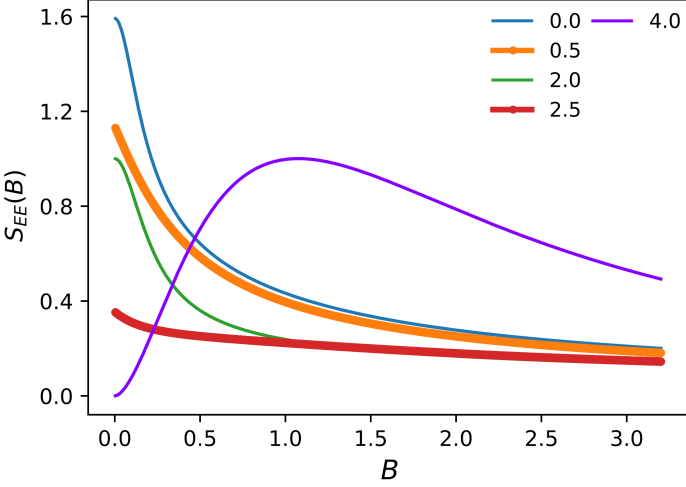


FIG. 18. Variation of the equipartition entanglement entropy for different CPI ground states and transition ground states (corresponding to different integer and half-integer values of $0 \leq \Phi \leq 4$) with the global $U(1)$ symmetry breaking field B for a system of $N^* = 8$ Cooper pairs. Note that the non-monotonic behaviour of the purple curve arise from the fact that this corresponds to the ground state precisely at the transition from the CPI to the parent metal.

is obtained for all these curves in the limit of large B , the approach of the mean-field ground state is clearly different from those with pre-existing Cooper pair bound states: the peak in the curve for $\phi = 4$ likely arises due to the creation of Cooper pairs in a gapless system.

B. The effect of a Josephson coupling

We end with a brief presentation of the effects of a Josephson coupling between the bulk of two CPI systems A and B (i.e., we are ignoring all effects from gapless edge states), each of which is modelled by H_{SB} (eq.(61))

$$\begin{aligned}
 H_\mu &= -\frac{2\epsilon_\mu}{V_\mu} \sum_{k \in \mu} S_k^z - \frac{V_\mu}{2N_\mu} \sum_{k \neq k' \in \mu} \left(S_k^+ S_{k'}^- + \text{h.c.} \right) \\
 &\quad - B_\mu \sum_{k \in \mu} S_k^x, \quad \mu=A,B \\
 H_{AB} &= T \sum_{k \in A, k' \in B} \left(e^{i\phi} S_k^+ S_{k'}^- + e^{-i\phi} S_k^- S_{k'}^+ \right), \quad (73)
 \end{aligned}$$

where H_{AB} is the Josephson coupling between the systems A and B, with the phase ϕ dependent on the externally applied voltage difference between the two systems⁶⁰. We have simulated the equations in eq.(73) for two systems comprised of 4 pseudospins each.

First, we set the field $B_A = 0$, such that system A is in a $U(1)$ symmetric CPI phase and couple it with the system B (H_B) for several values of the field B_B and the Josephson coupling T . The values of the parameters

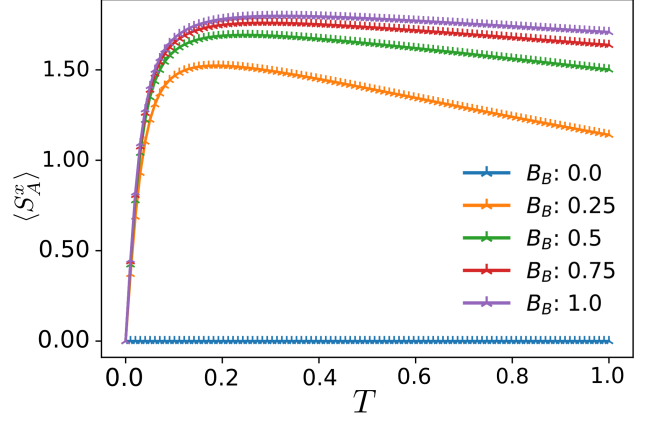


FIG. 19. Plot of the induced phase stiffness $\langle S_A^x \rangle$ in CPI system A due to a Josephson coupling (with strength T) to CPI system B (in presence of a global $U(1)$ symmetry breaking field (B_B)). Various curves correspond to different values of B_B .

$\epsilon_A = \epsilon_B =$, $V_A/N_A = V_B/N_B = 1$ and $\phi = \pi$. In Fig.19, we study the phase coherence being generated in the system A by computing $\langle S_A^x \rangle$ in the ground state of the total system ($H = H_A + H_B + H_{AB}$). The blue line in Fig.19 clearly shows that a Josephson coupling between two systems that are individually in CPI phases ($B_A = 0 = B_B$) cannot lead to phase coherence being induced in either system A or B. On the other hand, for non-zero values of B_B , the other curves in Fig.19 shows that as system B already possesses some degree of phase coherence, an increasing non-zero phase coherence is induced in system A via the Josephson coupling with increasing B_B . Note, however, that while this demonstrates the breaking of the $U(1)$ symmetry of the system A via the Josephson coupling to the symmetry-broken system B, the phases of the two systems are locked to one another with zero relative phase difference⁶⁰. This is demonstrated in a plot of the total ground state energy $E(\phi)$ as a function of the phase ϕ : the blue line in Fig.20 clearly shows that a Josephson current ($J \propto \partial E(\phi)/\partial \phi$) cannot be generated in the coupled system for $B_A = 0$. On the other hand, in the presence of a non-zero symmetry breaking field B_A , $E(\phi)$ shows a sinusoidal variation with ϕ in Fig.19. This shows that when the symmetry is separately broken in the two systems, a Josephson coupling certainly induces a Josephson current. The results of this subsection serve as predictions for the experimental search of systems in the CPI ground state.

VI. ENTANGLEMENT RENORMALISATION

Having explored the entanglement features of the topologically ordered CPI and symmetry broken BCS ground states at some length in previous sections, we now present an analysis the $T = 0$ RG evolution of the many-particle

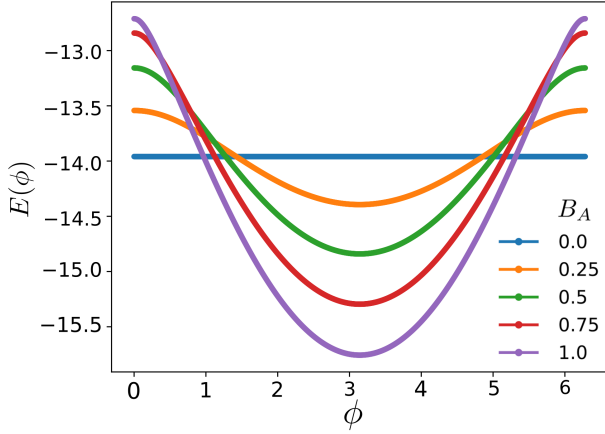


FIG. 20. Plot of the total ground state energy $E(\phi)$ for a CPI system (placed in a gradually increasing $U(1)$ symmetry breaking field B_A) coupled to a BCS superconductor through Josephson tunneling as a function of their phase difference ϕ . The various curves correspond to different values of B_A .

entanglement content of these ground states. For this, we follow the strategy for entanglement renormalisation that was developed in Refs.^{73,74}. For the sake of completeness, we outline briefly the strategy below. As we have seen earlier, the URG proceeds by disentangling electronic states sequentially from the UV towards the IR by the application of many-particle unitary transformations (U , see Appendix A for further details). At the IR stable fixed point, we have identified the ground state wavefunction. Now, by reversing the RG flow through the sequential applications of the appropriate U^\dagger s, we generate a family of ground state wavefunctions ranging towards the UV. This allows for the computation of several entanglement features from each member of the family of wavefunctions, thereby generating the RG flow of these entanglement features. As discussed in detail in Refs.^{73,74}, the unitary operators U of the URG method can be implemented as a quantum circuit, i.e., in terms of a combination of universal 2-qubit gates (e.g., Hadamard, C-NOT and phase-shift gates). Below, in Figs.21 and 22, we show the quantum circuit realisations that implement the reverse URG flow along one radial direction in k -space for the CPI and BCS wavefunctions respectively.

As shown in Fig.21, the nodes 9 and 19 refer to the fermion states residing just outside and just inside the Fermi surface respectively. The distance from the Fermi surface increases with passage between states 9 to 0 (all outside the Fermi surface), and with passage between states 19 to 10 (all inside the Fermi surface). As indicated by the quantum circuit diagrams, the reverse RG flow starts from the emergent CPI phase (described by

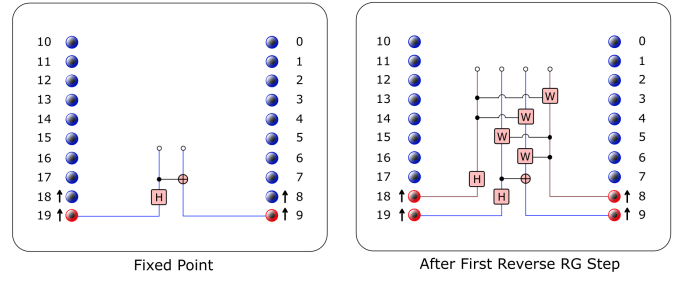


FIG. 21. Quantum circuit representation of (left panel) the ground state of the fixed point CPI Hamiltonian and (right panel) the ground state after the first step of the reverse unitary RG step. Both are for a system of $N^* = 2$ Cooper pairs.

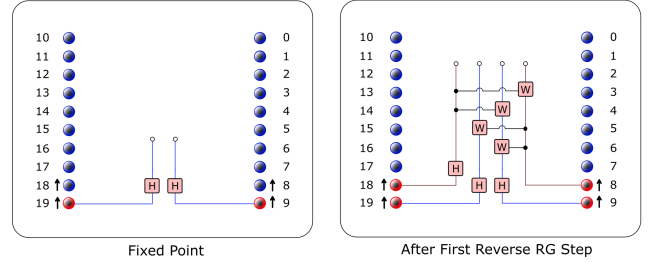


FIG. 22. Quantum circuit representation of (left panel) the ground state of the fixed point BCS Hamiltonian and (right panel) the ground state after the first step of the reverse unitary RG step. Both are for a system of $N^* = 2$ Cooper pairs.

the effective Hamiltonian in eq.(11)) obtained at the stable fixed point and with a window of electronic states given by N^* ($N^* = 2$ in the figures). The reverse RG flow proceeds by the re-entangling of two electronic states lying outside the window at each step of the RG. We now present the results of the RG evolution for the entanglement entropy of a block in k -space along a given radial direction for CPI and the symmetry broken phases. In Fig.23, we present the RG variation of the entanglement entropy computed for a block (lying outside the Fermi surface) of varying size ranging from one to ten fermionic states. The two plots are for different sizes of the window (N^*) for the emergent CPI phase: the upper plot is for $N^* = 2$ (i.e., comprised of states 9 and 19 only), while the lower is for $N^* = 8$ (i.e., comprised of state 6-9 and 16-19). Further, the reverse RG process increases stepwise from step 0 (in the IR) towards the UV.

The upper panel of Fig.23 shows that block entropy for all block sizes terminates at a universal value of $S = 0.693 = \ln 2$, corresponding to the entanglement for the $N^* = 2$ pseudospins that form the emergent CPI window in the IR. Further, the plots demonstrate that the block entanglement entropy of block size 1 (i.e., for the state 9, one of the two states that form the CPI ground state in the IR) increases slowly with the RG flow from

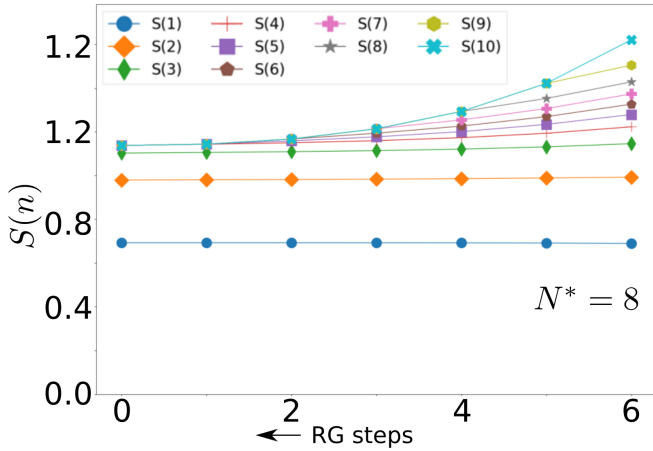
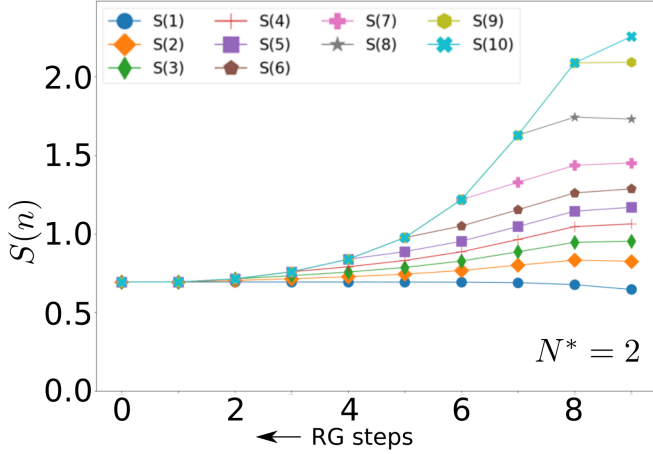


FIG. 23. Plot for the RG variation of the entanglement entropy $S(n)$ for various block sizes $1 \leq n \leq 10$ (in different colours) for a CPI system with $N^* = 2$ (upper panel) and $N^* = 8$ (lower panel) Cooper pairs. See text for discussion.

UV to IR. On the other hand, the block entropy of all other block sizes (greater than one) decreases with the stepwise decoupling of electronic states. Further, the entanglement entropy of the blocks varies non-linearly with the RG steps. Additionally, in the block entropy plots for $N^* = 8$ (lower panel of Fig.23), we see that the entanglement entropy for all block sizes less than 4 (i.e., the size of the four states 9-6 that are part of the CPI ground state in the IR) are affected very little by the RG flow. This is a remarkable display of the fact that the entanglement of the electronic states proximate to the Fermi surface (and that eventually form a part of the emergent window) is quite robust under RG evolution, and distinguishes them from those that are decoupled along the flow. Further, the CPI ground state possesses a hierarchy of scales of entanglement defined by the various block sizes.

Next, we present the entanglement RG results for a system in the presence of a bare symmetry breaking field

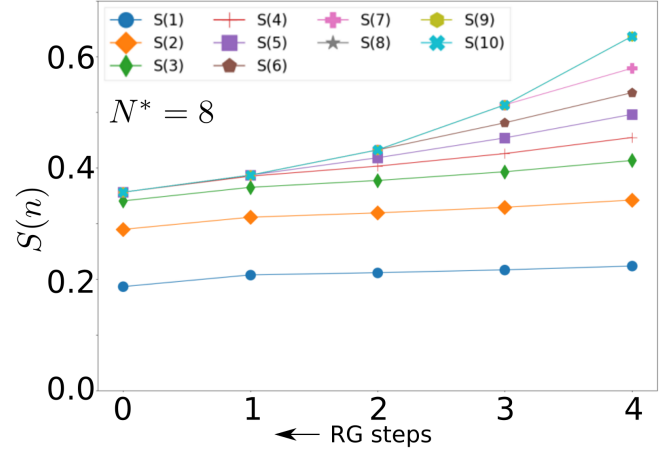
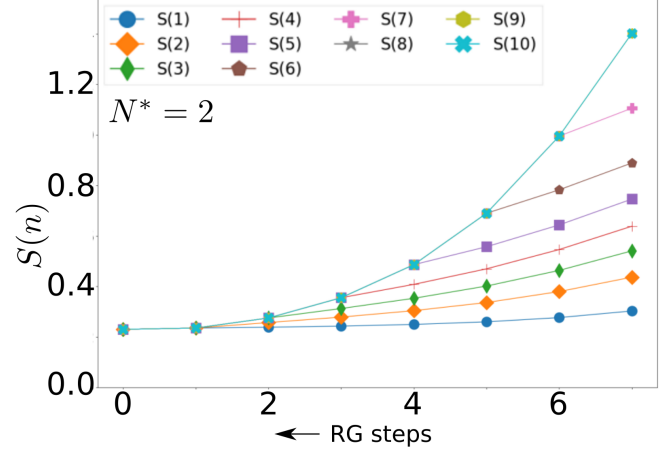


FIG. 24. Plot for the RG variation of the entanglement entropy $S(n)$ for various block sizes $1 \leq n \leq 10$ (in different colours) for a CPI system with $N^* = 2$ (upper panel) and $N^* = 8$ (lower panel) Cooper pairs in the presence of a weak global $U(1)$ symmetry breaking field $B = 5 \times 10^{-5}$ (in units of the attractive pairing coupling V). Note that the curves for $n = 8, 9$ and 10 are lying on top of one another. See text for discussion.

(B). In Fig.24, we see that the presence of a very weak bare $U(1)$ symmetry breaking field $B \sim 5 \times 10^{-5}$ (in units of V), the entanglement RG flows from UV to IR are very similar to those shown in Fig.23 above for the CPI (i.e. for the case of $B = 0$), with only one difference: the final value of the block entropies in the IR here is reduced with respect to those obtained for the CPI. This indicates a gradual collapse of the hierarchy of scales of entanglement of the CPI upon tuning a symmetry breaking field. Finally, in Fig.25, we present that the entanglement RG flows for a system with $N^* = 4$ for the case of a slightly larger (but still weak) bare $U(1)$ symmetry breaking field $B \sim 25 \times 10^{-3}$ (in units of V). Here, we find that the entanglement curves for various block sizes is very different to those obtained for the CPI (see Fig.23). For instance, the block entropy for both block sizes one and two (i.e.,

corresponding to the two possible subblocks of the emergent BCS ground state in the IR) have zero entanglement entropy throughout the RG. There is, thus, no longer any way to distinguish between the constituent blocks of the BCS ground state under the RG. Further, the entanglement entropy varies linearly with the RG steps for block sizes ≥ 8 .

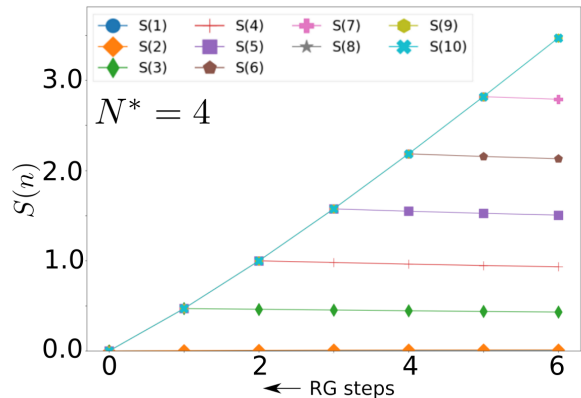


FIG. 25. Plot for the RG variation of the entanglement entropy $S(n)$ for various block sizes $1 \leq n \leq 10$ (in different colours) for a CPI system with $N^* = 2$ (upper panel) and $N^* = 8$ (lower panel) Cooper pairs in the presence of a strong global $U(1)$ symmetry breaking field $B = 25 \times 10^{-3}$ (in units of the attractive pairing coupling V). Note that the curves for $n = 8, 9$ and 10 are lying on top of one another. See text for discussion.

VII. CONCLUSIONS AND DISCUSSIONS

A body of theoretical work has proposed^{34,35,38}, on phenomenological grounds, the existence of a topologically ordered counterpart of the superconductor. This novel state of quantum matter, which we call the Cooper pair insulator (CPI) is expected to be a condensate of a fixed number of Cooper pairs, but without any phase stiffness. Instead, the CPI would correspond to a gapped system in the bulk and with gapless states at the boundaries. In keeping with this proposal, recent experimental studies of the superconductor to insulator transition (SIT) in thin films suggests the existence of such a CPI lying precisely at the transition^{9–11}. While the phenomenological gauge field theories proposed for the CPI offer some insight into its properties, a microscopic approach remains absent. Thus, a major finding of our work is the derivation of an effective microscopic Hamiltonian for the CPI that is emergent from a unitary renormalization group (URG) analysis.

For this, we have worked on a generalized model of a metallic system (i.e., with a repulsive density-density interaction U) as well as an attractive pairing interaction. Our URG study of this model offers a phase diagram in

terms of a quantum fluctuation scale (ω) and U , clearly displaying the existence of a CPI phase of quantum matter at small ω (i.e., corresponding to energyscales for excitations proximate to the Fermi surface) and for all U . The low energy fixed point effective Hamiltonian obtained for the CPI phase is then studied in detail. As mentioned earlier, the symmetry-preserved CPI phase is found to possess a fixed number of Cooper-pairs but without any global phase coherence among them. Subsequently, we have carried out a detailed analysis of various topological and many-particle entanglement features of this state of quantum matter, establishing thereby the emergence of topological order in the CPI. We have also contrasted the properties of the CPI ground state with its (BCS s-wave) superconducting counterpart, and believe that some of our results provide experimentally testable predictions. Importantly, we have also benchmarked numerically the ground state energy density of the CPI (in the thermodynamic limit) obtained from a finite-size scaling analysis for the RG against a similar finite size scaling analysis of exact diagonalisation calculations. We now end with a discussion of the broader significance of our findings with regards to the subject of topological order.

Topological order is proposed to describe the ordering of interacting many-particle quantum system beyond the Ginzburg-Landau-Wilson (GLW) paradigm (see Ref.⁷⁵ for a recent review). The GLW paradigm describes order arising the spontaneous breaking of symmetries, measured in terms of real-space local order parameters and associated with a phase transition whose universality is captured by a set of scaling exponents. On the other hand, a topologically ordered ground state does not arise from breaking any symmetries and thus lacks a local order parameter. Instead, such ground states are invariant under large gauge transformations, can be represented purely in terms of non-local gauge operators (e.g., Wilson loops etc.), and their quantum dynamics can be captured by a topological gauge field theory. When placed on a multiply connected manifold (e.g., a torus), a topologically ordered system displays a non trivial degeneracy of the ground state manifold (protected by a non-zero energy gap), as well as the existence of fractionally charged topological excitations that interpolate between the ground states. While the bulk of such a system is an incompressible insulating state of matter (due to the spectral gap), it can possess gapless current-carrying degrees of freedom at its boundaries. It has also been shown that the ground states of a topologically ordered system can possess signatures of non-trivial many-particle entanglement, e.g., an entanglement entropy (due to a real-space bipartitioning) proportional to the degeneracy count of the ground state manifold (called the quantum dimension). While all of these properties are widely believed to be the features and diagnostics of a topologically ordered system, an overarching theoretical framework for this subject remains an outstanding challenge. As the pairing instability of the Fermi surface represents

a paradigmatic phenomenon for a system of interacting electrons, our insights into the CPI represents an opportunity towards learning the inner workings of emergent topological order in such systems, as well as how it is different from the order captured by ground states belonging to the GLW paradigm (e.g., the BCS ground state). The body of results presented for the CPI phase clearly satisfy the diagnostics described above. We have established analytically the topological degeneracy of the ground state manifold using flux insertion arguments, and shown that the zero mode collective effective Hamiltonian for the CPI can be written in terms of Wilson loop operators. This then paves the way for connecting the topological θ term in the effective theory for the CPI with the 2+1 dimensional topological Chern-Simons gauge field theory proposed for such systems^{35,38,41}. We have shown the origin of the spectral gap that protects the ground state manifold, and shown the spectral flow property of such ground states with a variation in the θ parameter: ground states form plateaux in θ labelled by a topological quantum number and with topological quantum phase transitions separating them. Indeed, much of the phenomenology observed by us is common with the properties of topologically ordered fractional quantum Hall ground states (see Ref.⁷⁵ and references therein). It will be interesting to test these conclusions for systems of interacting electrons in the presence of disorder⁵⁰ or incommensuration^{76,77}.

Our investigations of the entanglement features show clear universal signatures that distinguish the topologically ordered CPI ground states (plateaux) from those found at the transitions between plateaux. The passage to the metallic state upon tuning the effective Aharonov-Bohm flux of the fixed point Hamiltonian is charted at zero as well as finite temperatures, yielding clear signatures once again in the entanglement for the CPI ground states. By carrying out the RG analysis in the presence of a global $U(1)$ symmetry breaking term, a detailed comparison between the CPI and BCS ground states is also offered. This allows us to demonstrate the clear distinctions between these two kinds of ground states in terms of many-particle entanglement and many-body correlations: unlike the BCS state, the CPI ground state is found to possess various measures of entanglement. Further, we show that, as CPI ground states lack phase stiffness, they cannot show the Josephson effect (i.e., upon coupling two such CPI systems through Cooper pair tunneling).

All of this leads us to conjecture that our results on the CPI offer a broad framework for understanding topological order. Specifically, we believe that various quantum liquid systems displaying the hallmark signatures of topological order described above are likely to be described by effective zero mode collective Hamiltonians described in terms of Wilson loop like non-local degrees of freedom. Using similar flux insertion arguments, it should be possible to show that the ground state manifolds of such Hamiltonians display topological degeneracy

on the torus etc. Indeed, similar conclusions have been reached by some of us for the Mott liquid ground states of the 2D Hubbard model discovered recently in Refs.^{46,47}, and the spin liquid ground states of quantum spins coupled through antiferromagnetic exchange on geometrically frustrated lattices^{48,78,79}. It should be possible, therefore, to chart out in a similar fashion the microscopic origins of various kinds of topologically ordered quantum liquids. This will go a long way in establishing a detailed understanding of the universality of such phenomena.

We end with a brief discussion on where to search for such CPI ground states. As we have seen here, the CPI state reached from a generic non-nested Fermi surface is strongly susceptible towards the effects of spontaneous symmetry breaking and the emergence of the BCS s-wave superconducting ground state. As mentioned earlier, some hints of the CPI have been found to lie at the superconductor to insulator transition in recent experiments on thin films. Based on our recent study of the 2D Hubbard model^{46,47}, and its relevance to the physics of the high-temperature superconducting hole doped cuprate Mott insulators, we believe that the CPI ground states may well be observed in those materials too. Specifically, in Refs.⁴⁷, we observed the existence at $T = 0$ of a pseudogapped CPI state of quantum matter lying above the d-wave superconducting “dome” obtained upon optimally doping the Mott insulating ground state of the 1/2-filled 2D Hubbard model with holes. This pseudogapped phase arose from electronic differentiation built into the electronic dispersion of the nested Fermi surface of the 2D tight-binding model at 1/2-filling. Further, the pseudogap phase showed a clear gapping of the anti-nodal regions in k -space that could be described in terms of a state of matter containing condensed Cooper pair bound states but without any global phase coherence. The large superconducting phase fluctuations observed in this pseudogapped phase⁴⁷ are a signature of the CPI, and are reminiscent of the findings from Nernst effect measurements on the pseudogap phase of the doped cuprates⁸⁰. We believe, therefore, that the cuprates are excellent candidate systems in which to search for the existence of the CPI phase. Following the suggestion of Ref.⁸¹, pressurised solid H_2S may be another interesting candidate system in which to search for the CPI.

ACKNOWLEDGMENTS

The authors thank A. Mukherjee, S. Pal, R. K. Singh, A. Dasgupta, A. Ghosh, S. Sinha, G. Baskaran, S. Moroz and A. Taraphder for several discussions and feedback. S. P. thanks the CSIR, Govt. of India and IISER Kolkata for funding through a research fellowship. S. L. thanks the DST, Govt. of India for funding through a Ramanujan Fellowship during which a part of this work was carried out.

Appendix A: Hamiltonian RG

We first briefly recapitulate the unitary RG method developed in Refs.⁴⁶⁻⁵¹, and then derive the RG equations for the generalised pairing Hamiltonian eq.(3). The RG method adopted uses a unitary transformation to decouple one single-particle Fock state $|k\sigma\rangle$ from the rest of the states it is interacting with. Very generally, one can write the many-particle Hamiltonian as $\hat{H} = \hat{H}^D + \hat{H}_{k\sigma}^X + \hat{H}_{k\sigma}^{\bar{X}}$, where \hat{H}^D contains all single-particle and many-particle number diagonal (kinetic energy and interaction) terms. $\hat{H}_{k\sigma}^X$ represents all the off-diagonal interaction terms connected to the single-particle state $|k\sigma\rangle$, while $\hat{H}_{k\sigma}^{\bar{X}}$ represents all off-diagonal interaction terms among all (say, 2^{N-1}) single-particle states other than $|k\sigma\rangle$. Considering a many-particle eigenstate of the Hamiltonian $|\Psi\rangle$ (a member of the full 2^N dimensional Hilbert space), we can write

$$\hat{H}|\Psi\rangle = (\hat{H}^D + \hat{H}_{k\sigma}^X + \hat{H}_{k\sigma}^{\bar{X}})|\Psi\rangle = \bar{E}|\Psi\rangle, \quad (\text{A1})$$

where \bar{E} is the eigenvalue for $|\Psi\rangle$. One can rewrite the wavefunction $|\Psi\rangle$ in a Schmidt decomposed form as follows

$$|\Psi\rangle = a_1|\Psi_1\rangle \otimes |1_{k\sigma}\rangle + a_0|\Psi_0\rangle \otimes |0_{k\sigma}\rangle, \quad (\text{A2})$$

where $\{|1_{k\sigma}\rangle, |0_{k\sigma}\rangle\}$ live in a 2-dimensional single-particle Fock space and $\{|\Psi_1\rangle, |\Psi_0\rangle\}$ lives in the remaining 2^{N-1} dimensional Hilbert space. We then proceed to remove all quantum fluctuations connected between $|k, \sigma\rangle$ with the other $|k' \neq k, \sigma\rangle$ states. For this, one can define transition operators $\hat{\eta}_{k\sigma}$ and $\hat{\eta}_{k\sigma}^\dagger$ as follows

$$a_1|\Psi_1\rangle \otimes |1_{k\sigma}\rangle = \hat{\eta}_{k\sigma}^\dagger a_0|\Psi_0\rangle \otimes |0_{k\sigma}\rangle, \quad a_0|\Psi_0\rangle \otimes |0_{k\sigma}\rangle = \hat{\eta}_{k\sigma} a_1|\Psi_1\rangle \otimes |1_{k\sigma}\rangle, \quad (\text{A3})$$

where $|1_{k\sigma}\rangle$ and $|0_{k\sigma}\rangle$ represent the $n_{k\sigma} = 1$ and $n_{k\sigma} = 0$ states respectively, and

$$\hat{\eta}_{k\sigma} = \frac{1}{\bar{\omega} - Tr_{k\sigma}(\hat{H}^D(1 - \hat{n}_{k\sigma}))(1 - \hat{n}_{k\sigma})} Tr_{k\sigma}(c_{k\sigma}^\dagger \hat{H} c_{k\sigma}). \quad (\text{A4})$$

Here, $Tr_{k\sigma}(\)$ represents a partial trace in the Fock space over the state $|k, \sigma\rangle$. These transition operators have a fermionic nature

$$\hat{\eta}_{k\sigma}^\dagger \hat{\eta}_{k\sigma} = \hat{n}_{k\sigma} = 1 - \hat{\eta}_{k\sigma} \hat{\eta}_{k\sigma}^\dagger, \quad \{\hat{\eta}_{k\sigma}^\dagger, \hat{\eta}_{k\sigma}\} = 1, \quad [\hat{\eta}_{k\sigma}^\dagger, \hat{\eta}_{k\sigma}] = 2\hat{n}_{k\sigma} - 1, \quad \hat{\eta}_{k\sigma}^2 = 0. \quad (\text{A5})$$

Using the transition operators $(\eta_{k\sigma}, \eta_{k\sigma}^\dagger)$ and the eqs.(A3), one can see that

$$\begin{aligned} |\Psi\rangle &= a_1|\Psi_1\rangle \otimes |1_{k\sigma}\rangle + a_0|\Psi_0\rangle \otimes |0_{k\sigma}\rangle \\ &= a_1|\Psi_1\rangle \otimes |1_{k\sigma}\rangle + \hat{\eta}_{k\sigma} a_1|\Psi_1\rangle \otimes |1_{k\sigma}\rangle \\ &= a_1(1 + \hat{\eta}_{k\sigma})|\Psi_1\rangle \otimes |1_{k\sigma}\rangle = a_1 e^{\hat{\eta}_{k\sigma}} |\Psi_1\rangle \otimes |1_{k\sigma}\rangle. \end{aligned} \quad (\text{A6})$$

Thus, one can construct a unitary operator

$$U_{k\sigma} = \frac{1}{\sqrt{2}}(1 + \eta_{k\sigma}^\dagger - \eta_{k\sigma}), \quad (\text{A7})$$

that rotates the many-particle basis in such way that $U_{k\sigma}|\Psi\rangle = \mathcal{N}|\alpha\rangle$, $\alpha = 0$ or 1 and \mathcal{N} normalization constant. This unitary rotation removes all quantum fluctuations between the states $|0_{k\sigma}\rangle$ and $|1_{k\sigma}\rangle$. Further, using the unitary operator, the Hamiltonian can be written in the rotated basis as

$$U_{k\sigma} \hat{H} U_{k\sigma}^\dagger = \frac{1}{2} Tr_{k\sigma}(\hat{H}) + \tau_{k\sigma} Tr_{k\sigma}(H \tau_{k\sigma}) + \tau_{k\sigma} \{c_{k\sigma}^\dagger Tr_{k\sigma}(\hat{H} c_{k\sigma}), \hat{\eta}_{k\sigma}\}. \quad (\text{A8})$$

It is important to note that while $\hat{n}_{k\sigma} \hat{H} (1 - \hat{n}_{k\sigma}) \neq 0$ (i.e., there existed non-trivial quantum fluctuations in the occupation of single-particle Fock state given by n_σ) prior to the application of the unitary operator, subsequent to its application we find

$$\hat{n}_{k\sigma} U_{k\sigma} \hat{H} U_{k\sigma}^\dagger (1 - \hat{n}_{k\sigma}) = 0 \Rightarrow [\hat{n}_{k\sigma}, U_{k\sigma} \hat{H} U_{k\sigma}^\dagger] = 0. \quad (\text{A9})$$

The degree of freedom $n_{k\sigma}$ is thus rendered an integral of motion (IOM) of the RG flow. The RG equations can then be obtained from the condition eq.(A9).

Coming to the problem at hand, in the generalised pairing Hamiltonian eq.(3), we are working in the subspace given by $n_{k,\sigma} = n_{-k,\sigma}$ ⁸². Thus, at every step of the RG, we are disentangling two single-particle states $|k, \sigma\rangle$, $|-k$ and $-\sigma\rangle$ simultaneously. We now proceed by rewriting the Hamiltonian in terms of Anderson pseudospins⁸²

$$H_{\text{pair}}^q = - \sum_k \tilde{\epsilon}_{k,q} (S_{k,q}^z - \frac{1}{2}) - \sum_{k \neq k'} \frac{|W_{kk'}^q|}{2} (S_{k,q}^- S_{k',q}^+ + \text{h.c.}) + U \sum_{k \neq k'} S_{k,q}^z S_{k',q}^z, \quad (\text{A10})$$

such that the part of the Hamiltonian associated with the k_N pseudo-spin is given by

$$H_N^q = -\tilde{\epsilon}_{k_N,q} \tau_{k,q}^z - \sum_{k \neq k_N} \frac{|W_{kk_N}^q|}{2} (\tau_{k_N,q}^- S_{k,q}^+ + \tau_{k_N,q}^+ S_{k,q}^-) + \frac{U}{4}. \quad (\text{A11})$$

Applying the RG formalism to H_N^q , one obtains from the condition eq.(A9) the operator level RG equation for the Hamiltonian in the low-energy sector for the quantum fluctuation scale ω as

$$\Delta H = \left(\sum_{k \neq k_N} \frac{|W_{kk_N}^q|}{2} \tau_{k_N}^+ S_k^- \right) G_{k_N} \left(\sum_{k' \neq k_N} \frac{|W_{k'k_N}^q|}{2} S_{k'}^+ \tau_{k_N}^- \right). \quad (\text{A12})$$

From this, we derive the RG equations in the relevant channel ($\tau_{k,q}^z = +\frac{1}{2}$) for Cooper pair condensation as

$$\frac{\Delta \tilde{\epsilon}_{k',q}^{(j)}}{\Delta \log \frac{\Lambda_j}{\Lambda_0}} = \frac{1}{4} \frac{|W_{k_\Lambda k'}^{(j)}|^2}{\left(\omega - \frac{\tilde{\epsilon}_{k_\Lambda,q}^{(j)}}{2} - \frac{U}{4} \right)}, \quad \frac{\Delta |W_{k'k''}^{(j)}|}{\Delta \log \frac{\Lambda_j}{\Lambda_0}} = -\frac{1}{4} \frac{|W_{k_\Lambda k'}^{(j)}| |W_{k_\Lambda k''}^{(j)}|}{\left(\omega - \frac{\tilde{\epsilon}_{k_\Lambda,q}^{(j)}}{2} - \frac{U}{4} \right)}. \quad (\text{A13})$$

Appendix B: URG with symmetry breaking field

We begin by including a global $U(1)$ symmetry breaking term ($-2|B| \sum_k S_k^x$) to the pairing Hamiltonian eq.(A10) (but with the repulsion coupling $U = 0$). Naturally, the symmetry breaking term now appears in the Hamiltonian involving the node k_N (eq.(A11)), as well as the operator RG equation (eq.(A12)). Subsequently, in the sector $\tau_{k_N}^z = +1/2$, we get the RG equations for $\tilde{\epsilon}_{k',q}$ and $|W_{k'k''}|$ precisely as in eqs.(A13) (but with $U = 0$). Further, we obtain a RG equation for the symmetry breaking field $|B|$

$$\frac{\Delta |B^{(j)}|}{\Delta \log \frac{\Lambda_j}{\Lambda_0}} = -\frac{1}{2} \frac{|B^{(j)}| |W_{k_\Lambda k''}^{(j)}|}{\left(\omega - \frac{\tilde{\epsilon}_{k_\Lambda,q}^{(j)}}{2} \right)}. \quad (\text{B1})$$

We now compute the spectral gap of the symmetry broken BCS superconducting phase. For this, taking $|W_{k_\Lambda k''}^{(j)}| \equiv W^{(0)}$ (a constant independent of k_Λ and k''), we note that the solution to the RG equation for B is given by

$$B^{(j)} = \frac{B^{(0)}}{1 + |W^{(0)}| \sum_{l=0}^{j-1} \frac{1}{2\epsilon^{(l)} - \tilde{\omega}}}. \quad (\text{B2})$$

The strong coupling RG fixed point of $B \rightarrow \infty$ is reached when the denominator of the above relation for B vanishes:

$$-\frac{1}{|W^{(0)}|} = \sum_l^{j-1} \frac{1}{2\epsilon^{(l)} - \tilde{\omega}} \approx \int_{E_F + \hbar v_F \Lambda^{(0)}}^{E_F + \hbar v_F \Lambda^*} \frac{N(E) dE}{2(E - E_F)}, \quad (\text{B3})$$

where we have replaced the sum by an integral, $N(E_F)$ is the electronic density of states (DOS) at the Fermi energy (E_F), $\epsilon^{(l)}$ by the continuous energy variable E and $\tilde{\omega}$ by $2E_F$. $\Lambda^{(0)}$ and Λ^* correspond to the bare and final k -space cutoffs of the RG flow. From here, we obtain the well-known relation for the (exponentially small) BCS gap

$$\Lambda^* = \Lambda^{(0)} \exp \left(-\frac{2}{|W_0| N(E_F)} \right). \quad (\text{B4})$$

* sp14ip022@iiserkol.ac.in

† slal@iiserkol.ac.in

- 1 L. N. Cooper, *Phys. Rev.* **104**, 1189 (1956).
- 2 J. Bardeen, L. N. Cooper, and J. R. Schrieffer, *Phys. Rev.* **108**, 1175 (1957).
- 3 V. L. Ginzburg and L. D. Landau, *Zh. Eksp. Teor. Fiz.* **20**, 1064 (1950).
- 4 X. M. Puspupus, K. H. Villegas, and F. N. C. Paraan, *Phys. Rev. B* **90**, 155123 (2014).
- 5 M. Di Tullio, N. Gigena, and R. Rossignoli, *Phys. Rev. A* **97**, 062109 (2018).
- 6 A. F. Hebard and M. A. Paalanen, *Phys. Rev. Lett.* **65**, 927 (1990).
- 7 A. Yazdani and A. Kapitulnik, *Phys. Rev. Lett.* **74**, 3037 (1995).
- 8 T. I. Baturina, D. R. Islamov, J. Bentner, C. Strunk, and M. R. B. . A. Satta, *Journal of Experimental and Theoretical Physics Letters* **79**, 337 (2004).
- 9 A. Doron, I. Tamir, S. Mitra, G. Zeltzer, M. Ovadia, and D. Shahar, *Phys. Rev. Lett.* **116**, 057001 (2016).
- 10 A. M. Goldman and N. Marković, *Physics Today* **51** (1998), doi: 10.1063/1.882069.
- 11 V. F. Gantmakher and V. T. Dolgoplov, *Physics-Uspexhi* **53**, 1 (2010).
- 12 S. L. Sondhi, S. M. Girvin, J. P. Carini, and D. Shahar, *Rev. Mod. Phys.* **69**, 315 (1997).
- 13 G. Sambandamurthy, L. W. Engel, A. Johansson, and D. Shahar, *Phys. Rev. Lett.* **92**, 107005 (2004).
- 14 H. Q. Nguyen, S. M. Hollen, M. D. Stewart, J. Shainline, A. Yin, J. M. Xu, and J. M. Valles, *Phys. Rev. Lett.* **103**, 157001 (2009).
- 15 M. Feigel'man, L. Ioffe, V. Kravtsov, and E. Cuevas, *Annals of Physics* **325**, 1390 (2010), july 2010 Special Issue.
- 16 *Nature* **449**, 876 (2007).
- 17 M. A. Paalanen, A. F. Hebard, and R. R. Ruel, *Phys. Rev. Lett.* **69**, 1604 (1992).
- 18 B. Sacépé, C. Chapelier, T. I. Baturina, V. M. Vinokur, M. R. Baklanov, and M. Sanquer, *Phys. Rev. Lett.* **101**, 157006 (2008).
- 19 Haviland, D. B., Y. Liu, and A. M. Goldman, *Phys. Rev. Lett.* **62**, 2180 (1989).
- 20 H. M. Jaeger, D. B. Haviland, B. G. Orr, and A. M. Goldman, *Phys. Rev. B* **40**, 182 (1989).
- 21 A. F. Hebard and M. A. Paalanen, *Phys. Rev. Lett.* **65**, 927 (1990).
- 22 van der Zant, H. S. J., Fritschy, F. C., Elion, W. J., L. J. Geerligs, and J. E. Mooij, *Phys. Rev. Lett.* **69**, 2971 (1992).
- 23 N. Mason and A. Kapitulnik, *Phys. Rev. Lett.* **82**, 5341 (1999).
- 24 N. Marković, C. Christiansen, A. M. Mack, W. H. Huber, and A. M. Goldman, *Phys. Rev. B* **60**, 4320 (1999).
- 25 M. A. Steiner, N. P. Breznay, and A. Kapitulnik, *Phys. Rev. B* **77**, 212501 (2008).
- 26 A. T. Bollinger, G. Dubuis, J. Yoon, D. Pavuna, and J. M. . I. Božović, *Nature* **472**, 458 (2011).
- 27 S. Eley, S. Gopalakrishnan, and P. M. G. . N. Mason, *Nature physics* **8**, 59 (2012).
- 28 A. Allain and Z. H. . V. Bouchiat, *Nature materials* **11**, 590 (2012).
- 29 Z. Han, A. Allain, H. Arjmandi-Tash, K. Tikhonov, M. Feigel'man, and B. S. . V. Bouchiat, *Nature physics* **10**, 380 (2014).
- 30 F. Couëdo, O. Crauste, A. A. Drillien, V. Humbert, L. Bergé, and C. A. M.-K. . L. Dumoulin, *Scientific Reports* **6**, 35834 (2014).
- 31 S. Park and J. S. . E. Kim, *Scientific Reports* **7**, 42969 (2017).
- 32 N. P. Breznay and A. Kapitulnik, *Science Advances* **3** (2017), 10.1126/sciadv.1700612.
- 33 C. G. L. Böttcher, F. Nichele, M. Kjaergaard, H. J. Suominen, J. Shabani, and C. J. P. . C. M. Marcus, *Nature physics* **14**, 1138 (2018).
- 34 D. Das and S. Doniach, *Phys. Rev. B* **60**, 1261 (1999).
- 35 M. Diamantini, P. Sodano, and C. Trugenberger, *Nuclear Physics B* **474**, 641 (1996).
- 36 M. Diamantini, P. Sodano, and C. Trugenberger, *Nuclear Physics B* **474**, 641 (1996).
- 37 M. Diamantini, A. Y. Mironov, S. Postolova, X. Liu, Z. Hao, D. Silevitch, Y. Kopelevich, P. Kim, C. Trugenberger, and V. Vinokur, *Physics Letters A* **384**, 126570 (2020).
- 38 T. Hansson, V. Oganessian, and S. Sondhi, *Annals of Physics* **313**, 497 (2004).
- 39 E. Fradkin and S. H. Shenker, *Phys. Rev. D* **19**, 3682 (1979).
- 40 E. Fradkin, *Field theories of condensed matter physics* (Cambridge University Press, 2013).
- 41 S. Moroz, A. Prem, V. Gurarie, and L. Radzihovsky, *Phys. Rev. B* **95**, 014508 (2017).
- 42 C. Dasgupta and B. I. Halperin, *Phys. Rev. Lett.* **47**, 1556 (1981).
- 43 M. P. A. Fisher and D. H. Lee, *Phys. Rev. B* **39**, 2756 (1989).
- 44 A. Vestergren, J. Lidmar, and T. H. Hansson, *Europhysics Letters (EPL)* **69**, 256 (2005).
- 45 P. W. Anderson, *Phys. Rev.* **112**, 1900 (1958).
- 46 A. Mukherjee and S. Lal, *New Journal of Physics* **22**, 063007 (2020).
- 47 A. Mukherjee and S. Lal, *New Journal of Physics* **22**, 063008 (2020).
- 48 S. Pal, A. Mukherjee, and S. Lal, *New Journal of Physics* **21**, 023019 (2019).
- 49 A. Mukherjee and S. Lal, *Nuclear Physics B* **960**, 115170 (2020).
- 50 A. Mukherjee and S. Lal, *Nuclear Physics B* **960**, 115163 (2020).
- 51 A. Mukherjee, S. Patra, and S. Lal, (2020), arXiv:2005.02332.
- 52 R. M. Fernandes and J. Schmalian, *Phys. Rev. Lett.* **106**, 067004 (2011).
- 53 C. Cao, M. van Caspel, and A. R. Zhitnitsky, *Phys. Rev. D* **87**, 105012 (2013).
- 54 H. Yao and D.-H. Lee, *Phys. Rev. B* **82**, 245117 (2010).
- 55 E. Lieb, T. Schultz, and D. Mattis, *Annals of Physics* **16**, 407 (1961).
- 56 M. B. Hastings, *Phys. Rev. B* **69**, 104431 (2004).
- 57 H. Lipkin, N. Meshkov, and A. Glick, *Nuclear Physics* **62**, 188 (1965).
- 58 N. Meshkov, A. Glick, and H. Lipkin, *Nuclear Physics* **62**, 199 (1965).
- 59 A. Glick, H. Lipkin, and N. Meshkov, *Nuclear Physics* **62**, 211 (1965).
- 60 J. van Wezel and J. van den Brink, *Phys. Rev. B* **77**, 064523 (2008).
- 61 ©Leiden University Press.
- 62 P. W. Anderson, *Phys. Rev.* **86**, 694 (1952).
- 63 J. van Wezel and J. van den Brink, *Physica B* **403**, 3206 (2008).
- 64 A. Mukherjee and S. Lal, (2020), arXiv:2003.06118.

- ⁶⁵ R. Micnas, J. Ranninger, and S. Robaszkiewicz, *Rev. Mod. Phys.* **62**, 113 (1990).
- ⁶⁶ J. Dukelsky, S. Pittel, and G. Sierra, *Reviews of modern physics* **76**, 643 (2004).
- ⁶⁷ P. Ribeiro, J. Vidal, and R. Mosseri, *Phys. Rev. E* **78**, 021106 (2008).
- ⁶⁸ X.-G. Wen and A. Zee, *Physical Review B* **46**, 2290 (1992).
- ⁶⁹ M. Oshikawa, *Phys. Rev. Lett.* **84**, 3370 (2000).
- ⁷⁰ M. Nakamura and J. Voit, *Physical Review B* **65**, 153110 (2002).
- ⁷¹ J. Eisert, M. Cramer, and M. Plenio, *Reviews of modern physics* **82**, 277 (2010).
- ⁷² J. I. Latorre, R. Orús, E. Rico, and J. Vidal, *Phys. Rev. A* **71**, 064101 (2005).
- ⁷³ A. Mukherjee and S. Lal, arXiv preprint arXiv:2003.06118 (2020).
- ⁷⁴ A. Mukherjee, S. Patra, and S. Lal, arXiv:2005.02332 (2020).
- ⁷⁵ X.-G. Wen, *Reviews of Modern Physics* **89**, 041004 (2017).
- ⁷⁶ Y. Hatsugai, *Phys. Rev. B* **48**, 11851 (1993).
- ⁷⁷ D. Sen and S. Lal, *Phys. Rev. B* **61**, 9001 (2000).
- ⁷⁸ S. Pal, A. Mukherjee, and S. Lal, *Journal of Physics: Condensed Matter* **32**, 165805 (2020).
- ⁷⁹ S. Pal and S. Lal, *Physical Review B* **100**, 104421 (2019).
- ⁸⁰ Y. Wang, L. Li, and N. Ong, *Physical Review B* **73**, 024510 (2006).
- ⁸¹ G. Baskaran, arXiv:1507.03921 (2015).
- ⁸² P. W. Anderson, *Physical Review* **112**, 1900 (1958).